TITANIUM-DOPED TUNGSTEN OXIDE FOR H$_2$S SENSORS:

SYNTHESIS, MICROSTRUCTURE AND PROPERTY EVALUATION

NARASIMHA RAJU KALIDINDI

Department of Mechanical Engineering

APPROVED:

_____

Chintalapalle V. Ramana, Ph.D., Chair

_____

Vinod Kumar, Ph.D.

_____

Felicia Manciu, Ph.D.

_____
Patricia D. Witherspoon, Ph.D.
Dean of the Graduate School

Copyright ©

by

Narasimha Raju Kalidindi

2010

Dedicated to my parents

TITANIUM-DOPED TUNGSTEN OXIDE FOR H$_2$S SENSORS:

SYNTHESIS, MICROSTRUCTURE AND PROPERTY EVALUATION

by

NARASIMHA RAJU KALIDINDI

THESIS

Presented to the Faculty of the Graduate School of

The University of Texas at El Paso

in Partial Fulfillment

of the Requirements

for the Degree of

MASTER OF SCIENCE

Department of Mechanical Engineering

THE UNIVERSITY OF TEXAS AT EL PASO

December 2010

UMI Number: 1483869

UMI

Dissertation Publishing

ProQuest®

ProQuest LLC
789 East Eisenhower Parkway
P.O. Box 1346
Ann Arbor, MI 48106-1346

Acknowledgements

I would like to express my deep and sincere gratitude to my advisor, Dr. C. V. Ramana, Ph.D., Department of Mechanical Engineering, University of Texas at El Paso. His wide knowledge and his logical way of thinking have been of great value for me. His understanding, encouraging and personal guidance have provided a good basis for the present thesis.

I am deeply grateful to Dr. Falicia, Ph.D., Department of Physical sciences, University of Texas at El Paso for her important support throughout this work and also Dr. Vinod Kumar, Ph.D., Department of Mechanical Engineering, University of Texas at El Paso, for serving on my thesis committee, and his valuable suggestions.

I would like to thank the Department of Mechanical Engineering for support and help during my two years of graduate study at UTEP. And I also want to thank the rest of the faculty in the department for educating me in my graduate courses of study at UTEP.

This work would not have been completed without the help and support of many individuals. I would like to thank everyone who has helped me along the way. Lastly, my family without whose support any of this would have been possible.

Abstract

Increasingly strict requirements for environment management of coal-generated waste streams are also anticipated with a growing incentive to reduce CO_2 production through increased efficiency. This planning model imposes demanding requirements for conversion of coal to electricity and to clean gaseous and liquid fuels and, thus, for a strategic program of research, development and commercialization to most efficiently utilize coal resource in the 21st century. Two very important goals that are proposed with their longer time horizon are increasing emphasis on clean fuels research and on advanced research that addresses the barriers to higher efficiency in both power generation and fuels production to reduce CO_2 emissions. Improvements will also be needed in control of air pollutants and the discharge of solid wastes. Our main focus in the present research is to detect the toxic and environmentally important gases that are released from a coal gasifier during the gasification process.

Metal oxide semiconductor gas sensors have been victoriously used to measure and monitor trace amounts of environmentally important gases such as CO, NO_2, H_2S, NH_3 and particularly challenging case of CO_2. Tungsten oxide (WO_3) has been successfully used as a gas sensor to detect very small amounts of gases up to a level of parts per million (ppm). Among the gases released, detection of H_2S, although present in very small amounts in crucial because it is extremely hazardous and toxic compound. In this work, the inhibition of WO_3 crystallization by the addition of Ti in sputter-deposited $W_{0.95}Ti_{0.05}O_3$ films is observed. The effect of growth-temperature on the crystallization indicates that the $W_{0.95}Ti_{0.05}O_3$ films grown at temperatures <300 °C are amorphous compared to WO_3 crystalline films at 100-200 °C. Phase transformation is induced in $W_{0.95}Ti_{0.05}O_3$ resulting in tetragonal structure at $\geq$300 °C. Segregation and formation of TiO2 is noted at 400-500 ^{o}C. The corresponding electrical properties and optical properties exhibit a clear distinction as a function of these structural transformations and TiO_2 formation.

Table of Contents

List of Tables

List of Figures

Chapter 1: Introduction

1.1 INTRODUCTION

The ever increasing demand for clean, renewable, efficient and affordable energy sets new stringent requirements for more energy production, storage, utilization and management. Energy production at a lower cost and reduced environment impact will, particularly, play a major role to meet the requirements of current and emerging needs in the energy sector. Ecological problems have become more severe primarily because of steadily increasing CO_2 emissions from fossil fuel burning plants, including those used for power production, transport, and industry (1). The ultimate global warming effect can cause dangerous climatic changes on Earth. Steadily increasing emissions of other atmospheric pollutants such as sulfur and nitrogen oxides are also very damaging to the environment. Reduction, through continuous monitoring and management, of all emissions from the energy systems, is therefore, of the utmost importance. These concerns create new challenges in the area of energy technology. The existing power production technology cannot fulfill these requirements in the most sensitive areas of efficiency and pollutant emissions. At present, energy technology is marked by tremendous efforts aimed at achieving higher efficiencies in energy conversion with reduced environmental impact and at lower costs. Although conventional energy technologies have been consistently improving in terms of efficiency, economics, and reduction of environmental impact in the last decade, modern power stations have achieved the ultimate degree of intrinsically limited efficiency. Further improvements are possible only by revolutionary changes of the energy technology. The 21st century will drastically change energy production and will become the era of more efficient combined power plants. The development trends are directed at the changeover from basically steam power technology to combined-cycle power based on such plants as gas turbines, fuel cells, MHD generators, as well as the advanced energy systems based on the utilization of renewable energy sources (2).

Gaseous fuels are the most sought-after raw materials and energy source in the energy economy. However, in the face of the state of world reserves of primary energy sources and the steadily rising demand for energy, it has become necessary to replace natural gas and oil by other energy sources to an increasing extent. It is estimated that a substitution of this kind will need to take effect before the turn of the century. The conversion of coal into a gaseous fuel and raw material will be of decisive importance in the attempts to secure the future of energy supplies.

Coal is one of the most widely used fossil fuels for production of power and industrial steam. In the foreseeable future, it is still expected to be utilized as a major source of fuel for power generation but there is an increasing need for clean-coal power generation for higher efficiency. One quarter of the world's coal reserves are found within the United States. Coal-fired electric generating plants are the cornerstone of America's central power system. The Integrated Gasification Combined Cycle (IGCC) technology is one key technology to provide an efficient and economic method for generating power from coal with substantially reduced emissions.

1.2 COAL GASIFICATION:

Coal gasification is a physio-chemical process, which converts coal from solid state to a gaseous state. Specifically, coal gasification refers to a process that breaks down coal into its components, by subjecting it to high pressure and high temperature in addition to the use of steam and oxygen (3). This leads to the production of synthesis gas, also called syngas which is mainly a mixture containing carbon monoxide and hydrogen. Three main routes can be followed for producing gas from coal on a large industrial scale. Processes involving pyrolysis are the most important, both quantitatively and economically. When coal is pyrolysed its volatile constituents are cracked to give gaseous and liquid products, which can be separated and worked up to provide marketable byproducts. Apart from the main syngas component, carbon monoxide, there are many other toxic gases present in a gasifier, particularly

2

if the end product is a chemical. Typical toxic gases present in syngas can include compounds such as H_2S and COS (carbonyl sulfide) as well as ammonia and HCN (4).

The majority of coal gasification processes are based on the interaction of carbon in coal with steam as the gasifying medium. The gasification process is endothermic, i.e. it occurs with heat absorption. The heat required for the coal gasification can be obtained through combustion (oxidation) of a relatively small quantity of coal with oxygen within the gasifier according to the following reactions of complete or partial oxidation of carbon with oxygen (4).

$$C + O_2 = CO_2 + 406 \text{ KJ/mol} \ldots\ldots\ldots\ldots\ldots (1)$$
$$C + \frac{1}{2}O_2 = CO_2 + 406 \text{ KJ/mol} \ldots\ldots\ldots\ldots (2)$$
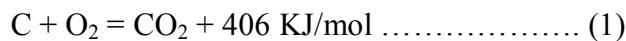
The gasification process consists of two stages. Coal pyrolysis, i.e. decomposition by heat, which occurs at high temperatures in the absence of air (oxygen), is the first. Some gas and liquids are produced from the volatile matter of coal, but the main product is a solid residue, i.e. char or coke. The coke gas may contain CO, H_2, CH_4, C_nH_m, H_2O, and CO_2. The amounts of gas and liquids depend on the coal rank and the temperature of the process.

Conversion of the products of pyrolysis to a product gas is the later. Fuel, e.g. coal or naphtha, and a gasifying medium are introduced into the gasifier. The product gas and the solid residual leave the gasifier. Usually steam is used as gasifying medium. Pure oxygen, oxygen, or air is supplied to the gasifier for partial oxidation of the original fuel. During gasification, certain heterogeneous (solid/gas) and homogeneous (gas/gas) reactions take place. They may be described as follows (3) (4).

The heterogeneous water-gas reaction is

$$C + H_2O \text{ (Steam)} = CO + H_2 \text{ } (\Delta H = +119 \text{ kJ/mol}) \ldots\ldots\ldots\ldots (3)$$
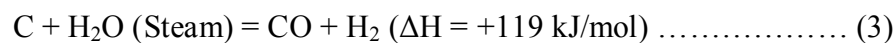
The heterogeneous Boudouard reaction is

3

$$C + CO_2 = 2CO \ (\Delta H = +162 \ KJ/mol) \ \ldots\ldots\ldots\ldots\ldots\ldots\ldots\ldots \ (4)$$
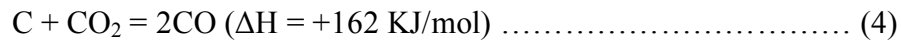
The homogeneous water-gas reaction is

$$CO + H_2O \ (steam) = H_2 + CO_2 \ (\Delta H = -42 \ KJ/mol) \ \ldots\ldots\ldots\ldots\ldots \ (5)$$
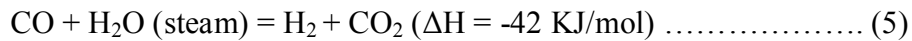
The homogeneous methanation reaction is

$$CO + 3H_2 = CH_4 + H_2O \ (\Delta H = -206 \ KJ/mol) \ \ldots\ldots\ldots\ldots\ldots\ldots \ (6)$$
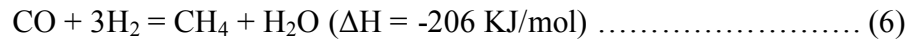
Total gasification process can be summarized as

Coal + gasifying medium (steam + oxygen or air) + heat =

Product gas ($CO + H_2 + CH_4 + CO_2 + N_2$) + refuse (slag, ash)

Although the gasification of coal was practiced as long as the 19th century and was developed to an advanced stage of technology in the first half of the present century, nowadays it is of importance only in a few countries with special economic conditions. The process of coal gasification offers many advantages over traditional coal combustion technology in terms of reduced emissions, thermal efficiency, and the ability to generate hydrogen or other high-value fuels or chemicals. In addition, coal gasification plants do not produce any scrubber sludge that needs careful and costly disposal. Another advantage of coal gasification is that coal ash from gasifiers is not hazardous and its leaching effect is low. An inherent environmental advantage of coal gasification over conventional pulverized coal fired power plants is the ease of sulfur removal in the former process. As hydrogen sulfide in gasification, sulfur is absorbed by an amine-based solvent in a vessel. Heating the solvent causes nearly chemically pure sulfur to separate from the solution. This virtually elemental sulfur can be sold commercially at a profit.

4
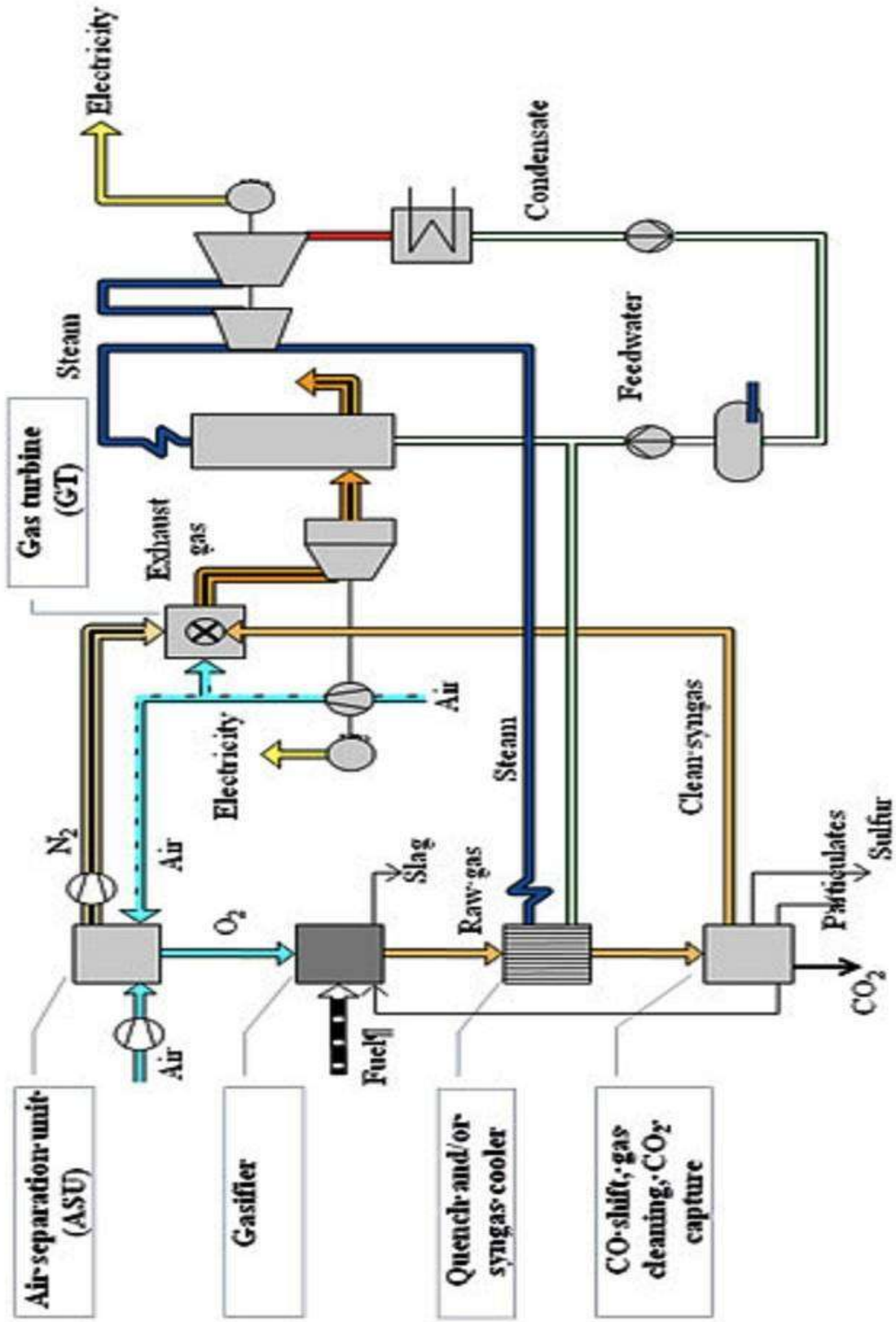
Figure 1.1: Siemens Integrated Gasification Combined Cycle Power Plant Layout

1.1.1 Integrated Gasification Combined cycle (IGCC):

Worldwide there are just four integrated gasification combined cycle (IGCC) plants running on coal today one in Spain, one in Netherlands, one in Indiana and one in Florida. So while technology is not new, our experience with commercial-scale IGCC plant is limited. There is still much to learn, particularly about the economics of operating a commercial-scale plant. IGCC is an innovative technology that combines modern coal gasification with a gas turbine and a steam turbine to produce electric power. It is one of the most promising technologies available today for reducing the environmental impacts associated with the use of coal for electricity production.

1.1.2 What are the advantages of IGCC technology?

Coal-fueled IGCC technology offers a number of potential benefits over conventional pulverized coal plants. Depending on the final configuration of the IGCC plant, these can include:

- Higher efficiency -the use of two turbines- a gas turbine and steam turbine-leads to higher efficiencies.
- Lower emissions -the gasification process enables improved removal of naturally-occurring pollutants in coal, such as sulfur and mercury, resulting in lower emissions that conventional coal based power plants.
- Carbon sequestration potential- the IGCC process makes easier to capture carbon dioxide for carbon sequestration.
- Marketable byproducts- the byproducts associated with gasification and gas clean-up process may have commercial value in nearby industries.

- Hydrogen as an alternative fuel source- Hydrogen is gaining popularity as a potential clean-burning fuel source of the future for vehicles and other industries. The ability to produce hydrogen from coal for such future applications could prove to be an important benefit of IGCC technology.

1.1.3 How do coal-based IGCC power plants work?

As illustrated in the figure below, IGCC power plants involve a complex chain of activities that start with a carbon-based material- in this case, coal- and result in electricity that powers our homes and businesses.

1. The coal gasification process begins with a controlled mixture of coal, oxygen and steam in a gasifier. An air separator unit separates air into its component parts to supply the gasifier with a stream of oxygen.

2. Using a combination of heat and high pressure, the gasifier converts the constituents of coal into a synthetic gas, or "syngas". This syngas is comprised of mostly hydrogen (H_2) and carbon monoxide (CO).

3. Byproducts captured in the gasifier could have commercial value, depending on local market conditions. For example, gasification plants produce an ash material similar to what comes from a traditional coal plants. This ash may be used as a filler material in construction projects and building products. Also in some coal gasifiers the ash may fall to the bottom of the gasifier as glass-like material, known as "Slag". This slag may be used in road gravel.

4. The syngas is then passed through a water gas shift reactor and reacted over a catalyst with added steam to convert the majority of the CO into carbon dioxide (CO_2) and additional H_2.

5. The syngas will also have small amounts of other impurities (e.g. hydrogen sulfide) which are removed during gas clean-up process.

6. Hydrogen sulfide will be separated from syngas and converted to elemental sulfur or possibly sulfuric acid. The sulfur byproducts may also have commercial value in the variety of products (e.g. fertilizer), depending on local market opportunities.

7. Most of the CO_2 is removed from the syngas leaving behind H_2 rich syngas.

8. One of the things that make IGCC plants more efficient is the combined use of a gas turbine and steam turbine to produce electricity. The hydrogen-rich syngas is first fed into a gas turbine to generate electricity. The waste heat from the gas turbine is used to power a steam turbine, which in turn creates more electricity.

9. Finally, much of the water used in the process will be recycled in the plant while some will be evaporated in a cooling tower.

1.3 H_2S GAS RELEASED DURING GASIFICATION:

Coal generally contains iron pyrite (FeS_2) and various divalent organic sulfurs, including, in descending order of thermal stability, thiophenes, aryl sulfides, cyclic sulfide, aliphatic sulfides, and aryl and aliphatic thiols (5). In a reducing atmosphere above about 500°C, iron pyrite reacts with hydrogen to form hydrogen sulfide (6). All the organic sulfur species present in coal can react with hydrogen to form hydrogen sulfide, with the reactivity of a species varying inversely with its thermal stability (5).

During pyrolysis of coal following reaction takes place to release hydrogen sulfide

$$FeS_2 + H_2 \quad \rightarrow \quad FeS \ + \ H_2S \ \ldots\ldots\ldots\ldots\ldots (7)$$
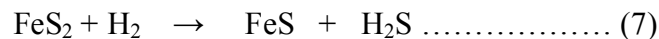
H_2S is the predominant gaseous contaminant in raw coal gas. It is commonly known as hydro sulfuric acid, stink damp and sewer gas. It smells like rotten eggs and people can smell it at low levels (less than 1 ppb) (7). Coal depending on the type and area of extraction can contain up to 5 wt. % sulfur, which is converted to gaseous H_2S during gasification. Problems arise due to the corrosive nature of H_2S

on metal components contained in these cycles. Because of this, H_2S concentrations must be reduced to low levels corresponding to certain power applications. For example, an integrated coal gasification combined cycle (IGCC) process producing electricity from coal at nearly 50% overall efficiency incorporates gas turbine that cannot tolerate H_2S levels above 100 ppm. Coal gasification/molten carbonate fuel-cell (MCFC) systems, achieving conversion efficiencies around 60%, function properly only if H_2S is below 1 ppm (8).

1.4 GAS SENSORS:

Gas sensors are sensing devices that interact with various gases and then provide the output to an instrument for displaying the measurements. Their applications are in toxic and combustible gas detection. The major gas sensor types are (9)

- Electrochemical

- Semiconductor

- Catalytic

- Infrared

Electrochemical sensors are mainly used to detect toxic gases, while catalytic and infrared sensors are used to detect combustible gases. They are also used for detecting the levels of oxygen. While detecting oxygen, they measure any reduction in the level of oxygen, and when detecting a toxic gas such as hydrogen sulfide, they look out for elevated levels of that gas (10).

There is a distinctly increasing demand for infrared gas sensors. These sensors are expected to register a higher growth rate as they do not get poisoned and have a longer lifetime. Catalytic gas

9

sensors are still preferred mainly due to the reluctance of some end users that are unwilling to shift to the infrared gas sensors.

However, electrochemical sensors are still the most preferred toxic gas sensor type and this trend is expected to continue (11). These sensors are inexpensive and reliable, which form their most important advantage over the other toxic gas sensor types such as semiconductor.

1.4 SEMI-CONDUCTOR METAL OXIDES FOR GAS SENSORS:

The idea of using semiconductors as gas sensitive devices dates back to 1952 when Brattain and Bardeen first reported gas sensitive effects on Germanium. Later, Seiyama found gas sensing effect on metal oxides. Taguchi finally brought semiconductor sensors based on metal oxides to industrial product. However, issues with sensitivity, selectivity, and stability have limited their use, often in favor of more expensive approaches. Recent advances in nanomaterials provide the opportunity to dramatically increase the response of these materials, as their performance is directly related to exposed surface volume. The recent availability of various metal oxide materials in high-surface-area nanopowder form, as well as implementation of newly developed nanofabrication techniques, offer tremendous opportunities for sensor manufactures (12).
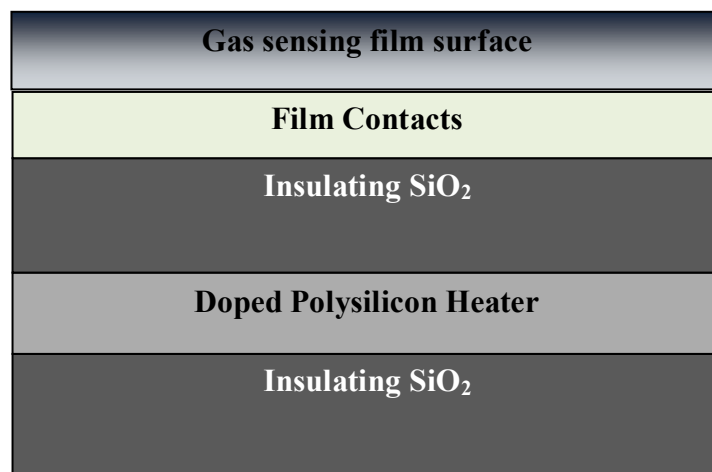
Gas sensing film surface
Film Contacts
Insulating SiO$_2$
Doped Polysilicon Heater
Insulating SiO$_2$

Figure 1.2: Crossectional view of a semiconductor sensor based on thin films

Many metal oxides are suitable for detecting combustible, reducing, or oxidizing gases by conductive measurements. The following oxides show a gas response in their conductivity: Cr_2O_3, Mn_2O_3, Co_3O_4, NiO, CuO, SrO, In_2O_3, WO_3, TiO_2, V_2O_3, Fe_2O_3, GeO_2, Nb_2O_5, MoO_3, Ta_2O_5, La_2O_3, CeO_2, and Nd_2O_3. Metal oxides selected for gas sensors can be determined from electronic structure. The range of electronic structures of oxides is so wide that metal oxides were divided into two following two categories (13):

(1)   Transition-metal oxides (Fe_2O_3, NiO, Cr_2O_3, etc.)

(2)   Non-transition-metal oxides, which include (a) pre-transition-metal oxides (Al_2O_3, etc.) and (b) post-transition-metal oxides (ZnO, SnO_2, etc.)

Pre-transition-metal oxides (MgO, etc.) are expected to be quite inert, because they have large band gaps. Neither electrons nor holes can easily be formed. They are seldom selected as gas sensor materials due to their difficulties in electrical conductivity measurements. Transition-metal oxides behave differently because the energy difference between a cation d^n configuration and either a d^{n+1} or d^{n-1} configurations is often rather small (14). They can change form in several different kinds of oxides. So, they are more sensitive than pre-transition-metal oxides to environment. However, structure instability and non-optimality of other parameters important for conductometric gas sensors limit their field of application. Only transition-metal oxides with d^0 and d^{10} electronic configurations find their real gas sensor application. The d^0 configuration is found in binary transition-metal oxides such as TiO_2, V_2O_5, WO_3. d^{10} configuration is found in post-transition-metal oxides, such as ZnO, SnO_2.

1.4.1 Band Theory Applied to Sensors:

Band theory as applied to gas sensors has been the subject of intense study for a number of years. The target gas interacts with the surface of the metal oxide film (generally through surface adsorbed oxygen ions), which results in a charge carrier concentration of the material. This change in charge carrier concentration serves to alter the conductivity (or resistivity) of the material (15). An n-type semiconductor is one where the majority charge carriers are electrons, and upon interaction with a

11

reducing gas an increase in conductivity occurs. Conversely, an oxidizing gas serves to deplete the sensing layer of charge carrying electrons, resulting in a decrease in conductivity. A p-type semiconductor is a material that conducts with positive holes being the majority charge carriers, hence the opposite effects are observed with the material and showing as increase in conductivity in the presence of an oxidizing gas (where the gas has increased the number of positive holes). A resistance increase with a reducing gas is observed, where the negative charge introduced in to the material reduces the positive (hole) charge carrier concentration (15). A summary of the response is provided in Table 1.

Table 1: Sign of resistance change (increase of decrease) to change in gas atmosphere

Classification	Oxidizing Gases	Reducing
n-type	Resistance increase	Resistance decrease
p-type	Resistance decrease	Resistance increase

1.4.2 Operating principle of a semi-conductor gas sensor:

The fundamental sensing mechanism of metal oxide based gas sensors relies on a change in electrical conductivity due to the interaction process between the surface complexes such as O^-, O_2^-, H^+, and OH^- reactive chemical species and the gas molecules to be detected. The general operating principle of a sensor is outlined in Fig. 1.3. A solid-state sensor consists of one or more metal oxides from transition metals, such a tin oxide, aluminum oxide, etc (13). Thick or thin film-chip sensors are made when the metal oxides are vacuum deposited onto a suitable substrate.

A heating element is used to regulate the sensor temperature, since the finished sensors exhibit different gas response characteristics at different temperature ranges. This heating element can be platinum or platinum alloy wire, a resistive metal oxide, or a thin layer of deposited platinum. The

sensor is then processed at a specific high temperature which determines the specific characteristics of the finished sensor.
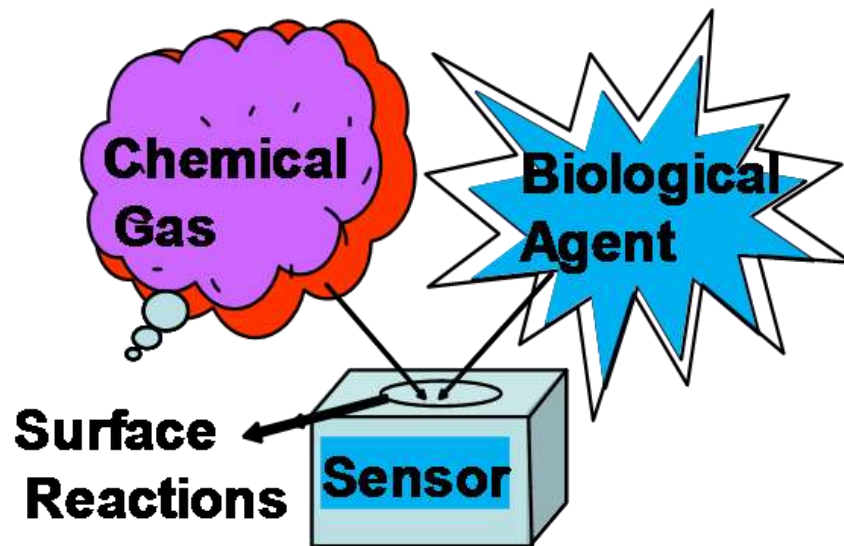
Figure 1.3: Operating principle of semiconductor sensor

In the presence of gas, the metal oxide causes the gas to dissociate into charged ions or complexes which results in the transfer of electrons. The built-in heater, which heats the metal oxide material to an operational temperature range that is optimal for the gas to be detected, is regulated and controlled by a specific circuit.

A pair of biased electrodes is imbedded into the metal oxide to measure its conductivity change. The changes in the conductivity of the sensor resulting from the interaction with the gas molecules are measured as a signal. Typically a solid-state sensor produces a very strong signal, especially at high gas concentrations. There are two types of adsorption: physisorption, the first step of the association of the gas species with the sensor surface, and chemisorptions, which involves exchange of electrons between the adsorbed species and the material surface This leads to the fact that physisorption predominates in low temperature range whereas chemisorption dominates in higher temperature range

13

1.4.3 Important Characteristics for the selectivity of a semi-conductor gas sensor:

Solid-state sensors are among the most versatile of all sensors, as they detect a wide variety of gases, and can be used in many different applications. Different response characteristics are achieved by varying the semiconductor materials, processing techniques, and sensor operating temperature. Among the unique attributes of the solid-state sensor are the abilities of the sensor to detect both low ppm levels of gases, as well as high combustible levels (16).

Longevity:

The main strength of the solid-state sensor is its long life expectancy, as the sensor typically lasts 10 years or more in clean applications. This is a major advantage compared to other sensor type, such as catalytic bead or electrochemical sensors, which typically last only one to two years.

However, while solid-state sensors have a longer life expectancy, they are also more susceptible to interference gases that the other type of sensors, thus, in applications where other background gases are present, solid-state sensors may trigger false alarms (17). In certain instances, the interferences from other gases are minimized by using appropriate filtering materials that absorb all other gases except the gas to be detected. For example, a solid-state sensor for monitoring carbon monoxide and hydrogen can be equipped with a charcoal filter which eliminates the majority of interfering gases. This way the sensor performs very well and becomes very selective for those two gases.

Versatility:

The versatility of the solid-state sensor is one of the main advantages. For example, in chemical plants, a gas monitoring system may involve the monitoring of many different gases and ranges, or even the same gas with multiple ranges. Often, the lower ranges need to be monitored for certain gases for toxic concentrations while simultaneously; the same gas needs to be monitored in the combustible range

14

for explosive concentrations. The solid-state sensor is capable of detecting gas in both ranges (18). This greatly simplifies the system design and maintenance required because it eliminates or minimizes the use of multiple sensor technologies which must be designed and maintained differently.

1.5 STRUCTURAL PROPERTIES OF TUNGSTEN OXIDE

Tungsten trioxide exhibits a cubic perovskite-like structure based on the corner sharing of WO_6 regular octahedra, with the O atoms (W atoms) at the corner (centre) of each octahedron (19). The crystal network can also be viewed as the results of alternating disposition of O and WO_2 planes, placed normally to each main crystallographic direction (Figure 1.4). This structure is also found in rhenium trioxide structure (ReO_3), from which takes its common name (ReO_3-structure). This structure is in itself rather uncommon. However, since it forms the base of perovskite (one of the most important ternaries), it has in fact chief importance.
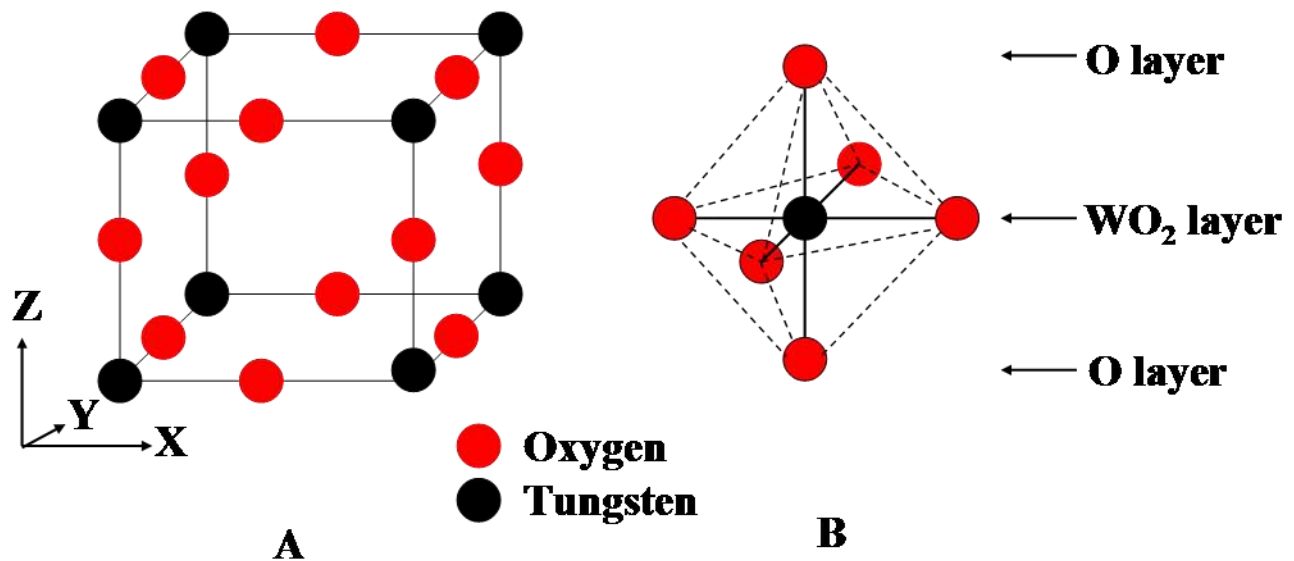

Figure 1.4: The structure of WO_3. (A) The ideal cubic structure of WO_3. (B) The WO_6 octahedra. The alternating WO_2 and O layers are also indicated (37).

Actually, the symmetry of tungsten oxide is lowered from the ideal ReO_3 structure by two distortions: tilting of WO_6 octahedra and displacement of tungsten from the centre of its octahedron. Variations in the details of these distortions give rise to several phase transitions (20). In fact tungsten trioxide adopts at least five distinct crystallographic modifications between absolute zero and its melting point at 1700 ºK. When the temperature is decreased from the melting point, the crystallographic symmetry for WO_3 changes in the sequence: tetragonal-orthorhombic-monoclinic-triclinic-monoclinic. Most of the transitions appear to be first order, and they often display large hysteresis in the transition temperatures. A summary of these transitions is given in Table 2 (14).

Another point worth noting is that the tungsten trioxide structure is likely to host several kinds of defects. One of the most elementary defects, as in most metal oxides, is the lattice oxygen vacancy, where an oxygen atom is absent from a normal lattice site (20). This leads to the formation of a family of WO_{3-x} compounds. From an electronic point of view, an oxygen vacancy causes the increase of the electronic density on the metallic (W) adjacent cations, leading to the formation of donor-like states slightly below the edge of the conduction band of the oxide, which acquires semiconducting properties (21).

Table 2: Known polymorphs of tungsten trioxide (adopted from (14))

Phase	Symmetry	Temperature Range (K)
$\alpha - WO_3$	Tetragonal	1010 – 1170
$\beta - WO_3$	Orthorhombic	600 - 1170
$\gamma - WO_3$	Monoclinic	290 – 600
$\delta - WO_3$	Triclinic	230 – 290
$\varepsilon - WO_3$	Monoclinic	0 - 230

Chapter 2: Experimental

2.1 SUBSTRATE CLEANING

The substrates used for all the experiments were p-type Si (100) wafers with the measured sheet resistance of 1.3 – 10 Ω-cm (measured by four point probe technique). Quartz and glass substrates were used in some selected experiments and as required by the type of measurement. In order to avoid contamination during deposition and to achieve high performance of devices fabricated, the silicon wafers are cleaned with RCA cleaning procedure to remove organic, inorganic and metal particulate contaminants.

The procedure for cleaning silicon wafers has three major steps:

- SC-1 - Removal of insoluble organic contaminants using 5:1:1 $H_2O/H_2O_2/NH_4OH$ solution

- SC-2 - Removal of ionic and heavy metal atomic components using a solution of 5:1:1 $H_2O/H_2O_2/HCl$ solution

- Removal of native oxide by buffered oxide etches solution.

The SC-1 solution was prepared by heating 50 ml of Deionized (DI) water to a temperature of 100 ºC and then adding 10 ml of NH_4OH and H_2O_2 each to the DI water. SC-2 solution was prepared by 10ml of H_2O_2 and HCl each to 50ml of water. The Si (100) substrates were soaked for 10 min in each solution and followed by 5 min of DI water rinse after each soak. Finally the silicon substrates were treated with BOE to remove any native oxide on it.

The glass and quartz substrates were used in some experiments, especially optical characterization, along with silicon substrates. These substrates were cleaned in an ultrasonic bath of

18

methanol (semiconductor grade), acetone (semiconductor grade), and DI water. The ultrasonic cleaning was carried out for 10 min in each step followed by a DI water rinse and then dried with nitrogen.

2.2 THIN FILM SYNTHESIS

W-Ti-O thin films in this work were grown employing radio-frequency (RF) magnetron sputtering. The sputter process involves bombardment of target material by ionized atoms, usually Ar^+ ions. The target material (called sputter target) is placed on a cathode and a negative voltage is applied to the cathode. The chamber is evacuated to high vacuum, usually 10^{-6} Torr and Ar gas will be injected into chamber at low pressures. The Ar gas will be ionized to create Ar^+ plasma. Ar^+ ions accelerate towards cathode, under the influence of cathode voltage, and bombard the target ejecting a target atom. The target atom will be deposited on to the substrate placed above the target. In this research RF magnetron sputtering was employed. In this type of sputtering a RF voltage of 13.56 MHz was applied to the target and the sputter cathode was equipped with a magnet.

A Kurt J Lesker sputter deposition system (Figure 2.1) has been used for the deposition. All the substrates were thoroughly cleaned and dried with nitrogen before introducing them into the vacuum chamber, which was initially evacuated to a base pressure of $\sim 10^{-6}$ Torr. Tungsten- titanium (W-Ti) alloy target (Plasmaterials Inc.) of 2 in. diameter and 99.95% purity was employed for reactive sputtering. The W-Ti alloy-target was placed on a 2 in. sputter gun, which is placed at a distance of 8 cm from the substrate. A sputtering power of 30 W was initially applied to the target while introducing high purity argon (Ar) into the chamber to ignite the plasma. Once the plasma was ignited the power was increased to 100 W, and pre-sputtered for 20 minutes by closing the shutter, to remove any contaminates present on the target surface. After pre-sputtering oxygen (O_2) was released into the chamber for reactive deposition. The flow of the Ar and O_2 and their ratio was controlled using as MKS mass flow meters. The deposition was carried out for 1 hr. The samples were deposited at different temperatures

19

varying from RT to 500 ℃ (in-situ heating). The substrates were heated by halogen lamps and the desired temperature was controlled by Athena X25 controller.
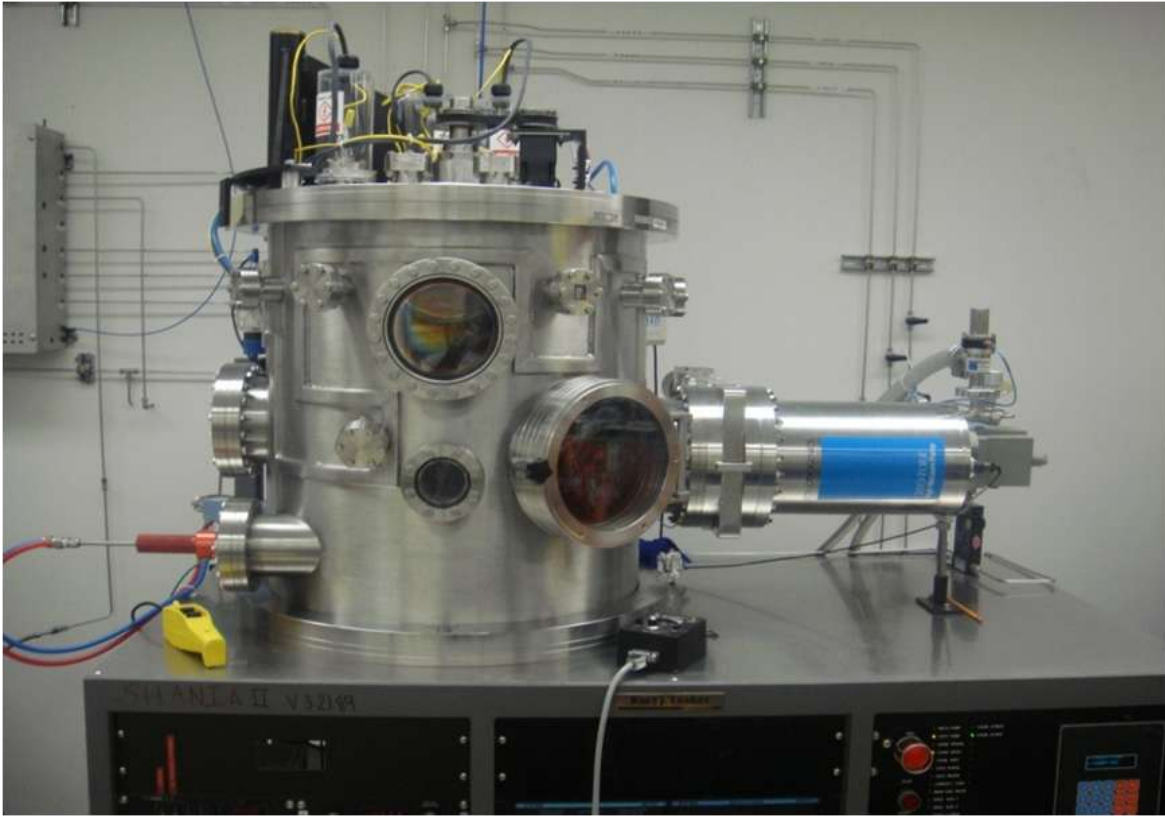
Figure 2.1: Kurt J Lesker R.F. Magnetron sputtering deposition system

2.3 CHARACTERIZATION

The WO$_3$ thin films obtained were characterized using High Resolution Scanning Electron Microscope (HRSEM), X-ray diffraction (XRD) and Optical Spectroscopy

2.3.1 Surface morphology and interface analysis

The films obtained have been characterized using a HRSEM for surface morphology and interface analysis. Surface morphology of the films gives information about the microstructure of the films while the interface analysis gives information regarding the films interaction with the substrate.

20

Table 3 : Deposition conditions

S.NO	Sample ID	Ar/O_2 Ratio	Ar Pressure	Total Pressure	Power (Watt)	Substrate Temp (ºC)	Deposition Time (min)
1.	W Ti 1	1:9	1.2*10E-3	6.1*10E-3	100	RT	60
2.	W Ti 2	1:9	1.2*10E-3	6.1*10E-3	100	100	60
3.	W Ti 3	1:9	1.2*10E-3	6.1*10E-3	100	200	60
4.	W Ti 4	1:9	1.0*10E-3	6.0*10E-3	100	300	60
5.	W Ti 5	1:9	1.0*10E-3	5.9*10E-3	100	400	60
6.	W Ti 6	1:9	1.0*10E-3	6.1*10E-3	100	500	60

Scanning electron microscope (SEM) uses an electron source with filament and anode. The microscopic column is contained in a vacuum envelope. As shown in the schematic below Figure 2.2, the incident electron beam is collimated, and then focuses onto the sample surface in a small spot. Then blanking and scanning coils are used to raster the spot across the sample. The signal from each spot on the surface is imaged at the display, keeping the same raster position as the spot on the sample. In this way an image is formed from the interaction of the incident electron beam at each position on the sample surface. The HRSEM used for this work is a Hitachi S-4800 electron microscope (Figure 2.3).

Magnification is achieved by rastering over a smaller area and displaying the smaller raster area on the entire screen. Incident beam size and the interaction area at the surface determine the resolution. Secondary electrons emitted from the sample surface as a result of collisions with the incident electron beam are used to form the image. The contrast in the image arising from the secondary electrons is due to the yield of the secondary electrons from each point probed on the sample surface. A particular point on the surface may contain atoms that yield more secondary electrons from an incident electron dose than an adjacent spot, and this spot will have a brighter image than the adjacent spot.

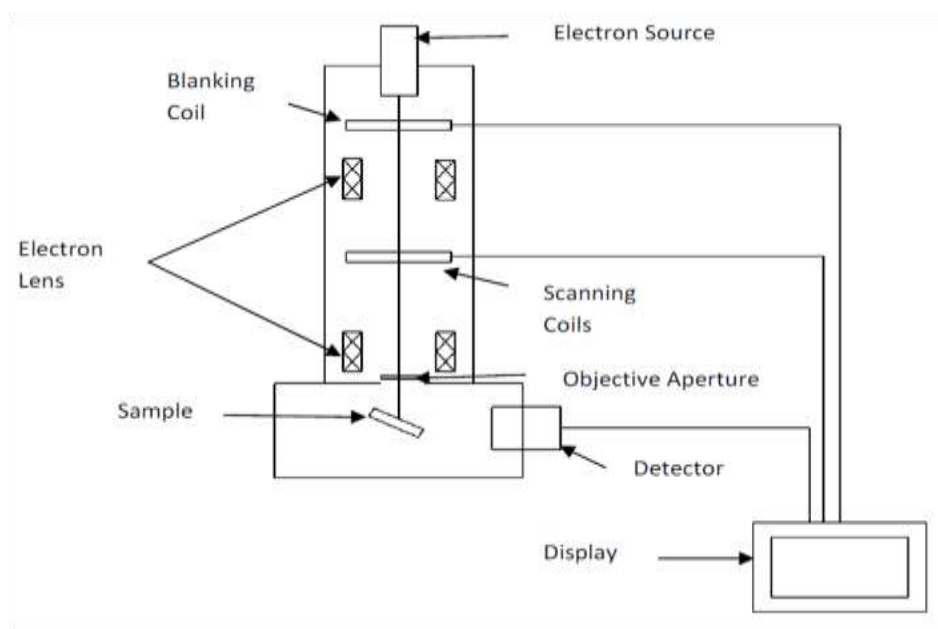Figure 2.2: Schematic sketch of an SEM showing major components

To obtain the image of the surface the sample is placed on a stage with its film surface facing the beam. For the interface image, the sample is placed in such a way that both the film and the substrate (cross- section) face the beam. The grain size and thickness of the film can be determined from the images by using image analysis software.

Figure 2.3: Hitachi S-4800 Scanning Electron Microscope

2.3.2 Structural characterization

A Bruker D8 Advance X-Ray diffractometer (XRD) (Figure 2.4) has been used for the structural characterization. The crystal structure preferred crystallographic information (if any), crystallite size, and the phases were determined from XRD patterns. XRD is an analytical technique in which x-ray beam hits the surface of a substrate at various incident angles scattering preferentially oriented x-rays into detector which collects them to generate crystallographic information about the sample such as lattice parameter, d-spacing, film orientation. XRD principle is based on Bragg's law

$$\lambda = 2d \sin \theta \dots\dots\dots\dots\dots\dots\dots (8)$$

Where λ = wave length of X-ray, d = inter planar distance and

θ = Bragg's angle.

23

Figure 2.3: Bruker D8 Advance X-ray diffractometer

2.3.3 Optical characterization

The samples obtained have been characterized using a Cary 5000 UV-VIS-NIR optical spectrophotometer (Figure 2.5) in the wavelength range of 200–2000 nm. The optical characterization is usually performed on highly transparent and semi-transparent thin films deposited on transparent substrates such as quartz.

The transmittance data obtained for the samples is used for calculating the band gap.

First, the absorption coefficient α is determined using the thickness of the film (t) and transmittance data (T) from the formula

$$\propto = \ (-\ln{(T)})/t \ \text{.................................} \ (9)$$

24

The energy of the photons hυ is calculated at every wavelength (λ) of light using the equation

$$h\upsilon = \frac{1240}{\lambda} \quad \text{(10)}$$

The band gap of the films is then measured using the equation

$$\alpha h\upsilon = B(h\upsilon - E_g)^2 \quad \text{(11)}$$

Where B is proportionality constant and E_g is the band energy, the band gap of the films are calculated by plotting a graph between ($\alpha h\upsilon^{1/2}$ vs. hυ. The transmittance data can further be used to calculate the extinction coefficient k, refractive index n and dielectric constants.
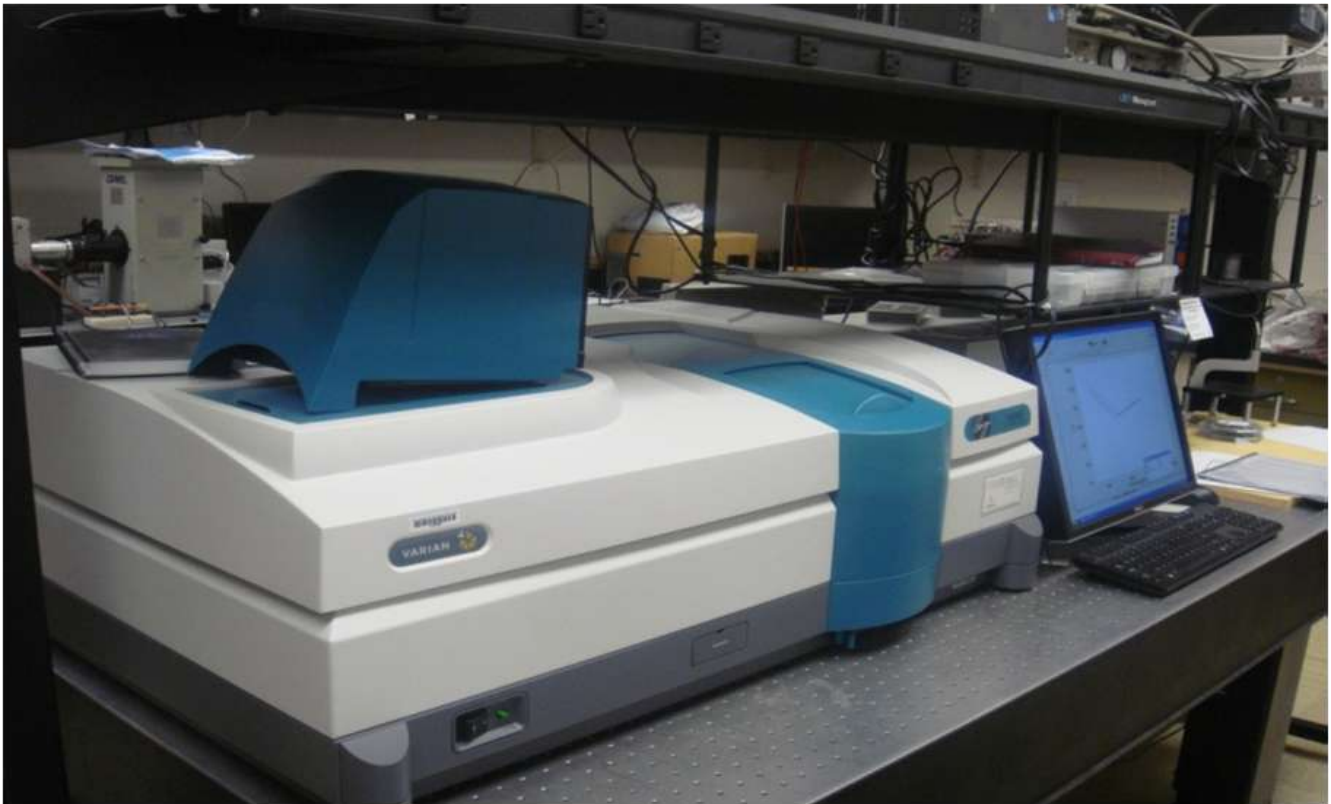

Figure 2.5: Cary 5000 UV- VIS – NIR spectrophotometer

Chapter 3: Literature Review

3.1 HISTORY OF TUNGSTEN OXIDE WO₃

Since Seiyama and Taguchi used the dependence of the conductivity of ZnO on the gas present in the atmosphere for gas sensing applications (22), (23)many different metal oxides have been proposed for gas detection. Generally speaking, these oxides can be divided into binary oxides and more complex oxides, being the former much more common in gas sensing applications.

Among binary metal oxides, tin dioxide (SnO_2) is the one that has received by far more attention since Taguchi built the first tin oxide sensor for Figaro Sensors in 1970 (24). This is probably due to its high reactivity to many gaseous species. However, this characteristic has also revealed as a lack of selectivity, and thus investigation on the other metal oxides has been considered necessary. Besides, developers of electronic noses have experimented with arrays of different sizes that may include around ten MOX sensors (25), apart from other types of chemical sensors. The use of different MOX sensors is highly recommended in order to increase the amount of information.

3.2 GAS SENSORS BASED ON TUNGSTEN OXIDE:

In recent years, significant number of groups has been working on tungsten oxide, which was highly appreciated in the field of MOX gas sensors. In practice, these contributions have been showing that tungsten trioxide is an interesting material for the detection of mainly three gases: ammonia, hydrogen sulfide and nitrogen dioxide (26). Investigations indicate that, sensor response of tungsten oxide to these gases can be, at least, as good as the sensor response exhibited by tin oxide, if not higher. Moreover, tungsten oxide has revealed as low sensitive to carbon monoxide and hydrocarbons, what makes it more interesting for the detection of these gases.

26

Prof. Yamazoe has mainly investigated pure tungsten oxide, although paying attention to more characteristics than just sensor response, such as mobility (27), film microstructure (28) and stoichiometry (29). These authors have concluded that activated 500 Å Au-doped WO_3 films have been found to be stable, sensitive and selective elements. Their films showed no ageing effects and were sensitive to 1 ppb of hydrogen sulfide at 200 ˚C. The authors argue that, in the case of their WO_3-sputtered sensitive films, post deposition annealing of the films to 400 ˚C in air induced crystallization, an increase in surface roughness and a decrease in film conductivity (30). This crystallization process markedly improved the sensitivity and response of the WO_3 films to hydrogen sulfide (31). In (32), the authors explain that differences in response behavior to H_2S gas between films containing the tetragonal versus the monoclinic phase suggest that oxygen vacancy and charge transport mechanisms are dependent on film microstructure.

Other groups have investigated the introduction of a metal such as Ti (33), although little attention has been paid to understand the effects of this addition.

Prof Cantalini and his group have contributed with more fundamental works on structural properties of WO_3 (34). According to them, in order to achieve a small grain size, the paramount factor is the annealing temperature, rather than the annealing time. Actually, kinetic solid-state sintering models have highlighted the exponential dependence of the rate of crystal growth with the sintering temperature, compared with only a linear dependence with sintering time (35). Since sensor response is reported to decrease with increasing grain size, the authors propose to fix the annealing temperature at the crystallization temperature of the material (300 ˚C in the case of WO_3) (36). On the other hand, these authors claim annealing time has a positive effect in improving the long-term stability of the sensors. During annealing, an adjustment of the surface or grain boundary defects to their equilibrium state takes

27

place, being this process time-dependent. Long annealing times are required if low annealing temperatures are chosen (37).

Finally, there is always an optimum operating temperature that corresponds to the highest reaction rate of the gas. However, the operating temperature must always be lower than the annealing temperature to achieve stability. If the optimum temperature is over the crystallization temperature, annealing temperature must be risen (38).

The study of the micro structural properties of a W–Ti–O thin film suitable to gas sensing has led to some important results. SEM and TEM analyses highlighted the features of the layer after annealing at either 600 or 800 °C (39). Annealing the films at 600 °C result in a sensing layer which has enhanced sensitivity to NO_2 compared to pure-WO_3 films. The fine granularity of the continuous layer determines its conducting properties and explains the high sensitivity of the material. This feature is ascribed to the solution of Ti ions in the WO_3 lattice, which impedes formation of coarse-grained structures (40). Pure WO_3 segregation as insulated crystallites, which do not affect significantly the sensing characteristics, suggests that future depositions should be carried out from a sputtering target richer in Ti (41). Annealing at 800°C produces a thin film of TiO_2 anatase with nanosized structure only partially covered with large WO3 crystallites (42). The high surface-to-volume ratio and nanogranularity envisage an exploitation of this material as a gas sensor for NO_2 detection in the temperature range of 350–800 °C with no interference from CO and NH_3 (43). Finally they mentioned that reactive sputtering followed by annealing at 800 °C of the sample is also a novel method to produce thin films of nanostructured TiO_2 anatase, stable up to 800 °C, with reproducible and relatively easy technique a feature that could be used in several fields other than chemical sensors (44).

Chapter 4: Results and Discussion

The emphasis in this work is to characterize the growth behavior, microstructure, and electronic properties of sputter-deposited $W_{0.95}Ti_{0.05}O_3$ materials as a function of growth temperature (T_s) and establish the conditions to produce high quality materials for H_2S sensor application. For this purpose, $W_{0.95}Ti_{0.05}O_3$ films were grown at various deposition conditions and studied their structural, morphological, optical and electrical properties. Samples were grown at varying temperature by maintaining a constant reactive gas ratio of 1:9 to study the effect of temperature. The results obtained are presented and discussed below in the following sequence. The crystal structure and phase analysis is made based on the XRD results and their analysis. The compositional or phase stability of $W_{0.95}Ti_{0.05}O_3$ films is examined considering the EDS data. Subsequently, the focus is on SEM data to discuss the effect temperature on the grain structure and morphology. Based on the microstructure and phase analysis, a phase diagram indicating the structure evolution as a function of growth temperature in $W_{0.95}Ti_{0.05}O_3$ films is established (Figure 4.5). Finally, the observed dependence of optical and electrical properties on the growth temperature is explained on the basis of the relative structural changes in the oxide films. An attempt is made to establish a correlation between growth conditions, microstructure, and electronic properties of the grown $W_{0.95}Ti_{0.05}O_3$ materials which can provide a road-map to select the specific conditions for H_2S sensor applications.

4.1 CRYSTAL STRUCTURE

The XRD patterns of $W_{0.95}Ti_{0.05}O_3$ films are shown in Figure 1 as a function of T_s. The XRD curve (Figure 4.1) of $W_{0.95}Ti_{0.05}O_3$ films grown at T_s=RT-200 ºC did not show any peaks indicating their characteristic amorphous (a-$W_{0.95}Ti_{0.05}O_3$) nature. The diffraction peak begins to appear in XRD pattern when T_s=300 ºC indicating the film crystallization at this temperature. The intense peak corresponds to the tetragonal phase of WO_3 indicating that the $W_{0.95}Ti_{0.05}O_3$ films crystallize in tetragonal structure.

The crystallization temperature noted for Ti-doped WO_3 films is higher when compared to that of pure WO_3 films grown using sputter-deposition. We reported previously that pure WO_3 films crystallize at T_s=100-200 ºC (45), (46). The effect of Ti is remarkable in preventing crystallization of WO_3 and raises its crystallization temperature.
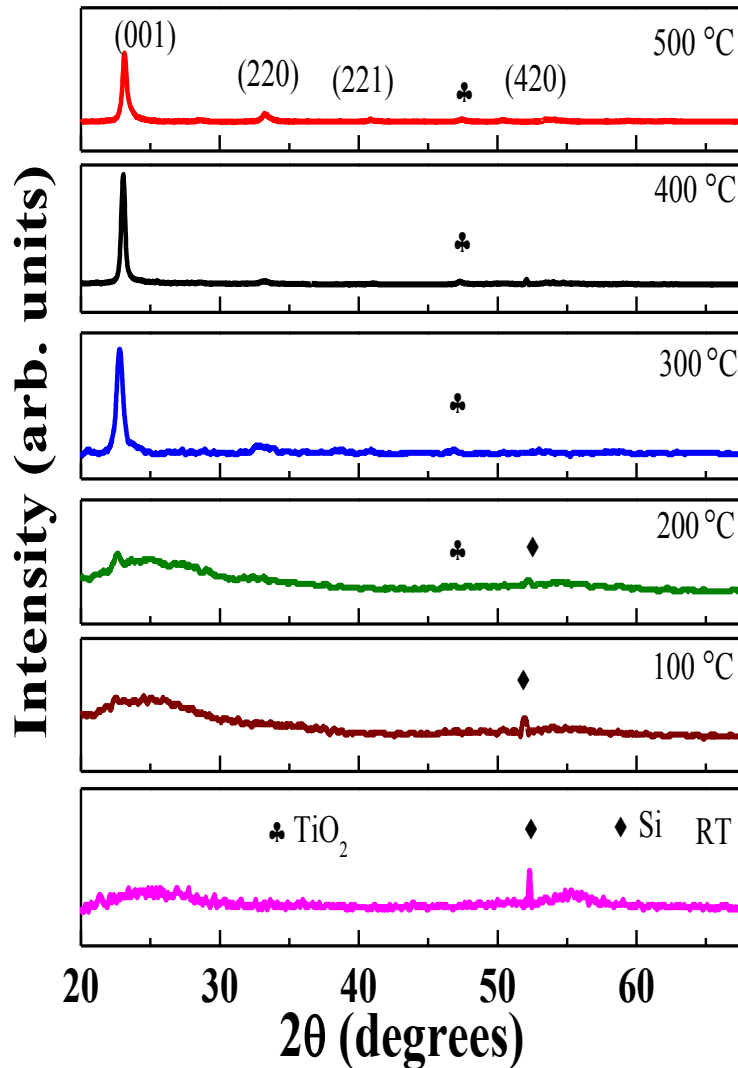

Figure 4.1: XRD patterns of $W_{0.95}Ti_{0.05}O_3$ films. It is evident from the curves that the films grown at RT, 100 ºC, 200 ºC are amorphous whereas films grown at Ts ≥300 ºC are nanocrystalline, crystallize in tetragonal phase.

The XRD peak is rather broad indicating the presence of nanocrystallites. It is evident (Figure 4.1) that the intensity of the peak which corresponds to diffraction from (00l) planes increase with increasing T_s. This is indicative of an increase in the average crystallite-size and preferred orientation of

30

the film along (00l) with increasing T_s. This behavior is quite similar to that observed in pure WO_3 films [7]. The preferred c-axis orientation of $W_{0.95}Ti_{0.05}O_3$ films could be due to the growth process minimizing the internal strain-energy in the film. Anisotropy exists in crystalline materials and the strain energy densities will typically be different for different crystallographic directions (47). The growth will favor those orientations with low strain energy density. Therefore, increasing T_s favors the preferred orientation along (00l) while minimizing the strain-energy in the $W_{0.95}Ti_{0.05}O_3$ films. The most important feature that can be noted is the formation of a small amount of TiO_2 phase for the films grown at T_s=400-500 ºC. Note that the peak becomes broad at T_s=500 ºC.

4.2 SURFACE MORPHOLOGY

The high resolution SEM images of $W_{0.95}Ti_{0.05}O_3$ films as a function of substrate temperature are shown in Figures 4.2. The effect of temperature on the surface morphology of $W_{0.95}Ti_{0.05}O_3$ films is remarkable. As it is evident from these images, the SEM data of $W_{0.95}Ti_{0.05}O_3$ films can be divided into two categories where the morphology differences are significant. The first category contains the set of $W_{0.95}Ti_{0.05}O_3$ films grown at temperatures < 200 ºC (Figure 4.2 (a), (b)). The second is the set of $W_{0.95}Ti_{0.05}O_3$ films grown at temperatures >200 ºC (Figure 4.2 (c), (d), (e), (f)). No features can be seen for $W_{0.95}Ti_{0.05}O_3$ films grown at RT and 100 ºC even at very high magnifications (Figure 4.2(a), (b)). This observation is in agreement with the XRD results indicating the complete amorphous nature of the samples. If temperature is low such that the period of the atomic jump process of ad atoms on the substrate surface is very large, the condensed species may stay stuck to the regions where they are landing thus leading to an amorphous $W_{0.95}Ti_{0.05}O_3$ film. The ad atom mobility on the surface increases with increasing temperature (47). The SEM images of $W_{0.95}Ti_{0.05}O_3$ films grown at T_s>200 ºC are shown in (Figure 4.3(c), (d), (e), (f)). A fine microstructure and uniform distribution of dense particles spherical in shape can be seen in $W_{0.95}Ti_{0.05}O_3$ films grown at T_s=300-500 ºC.
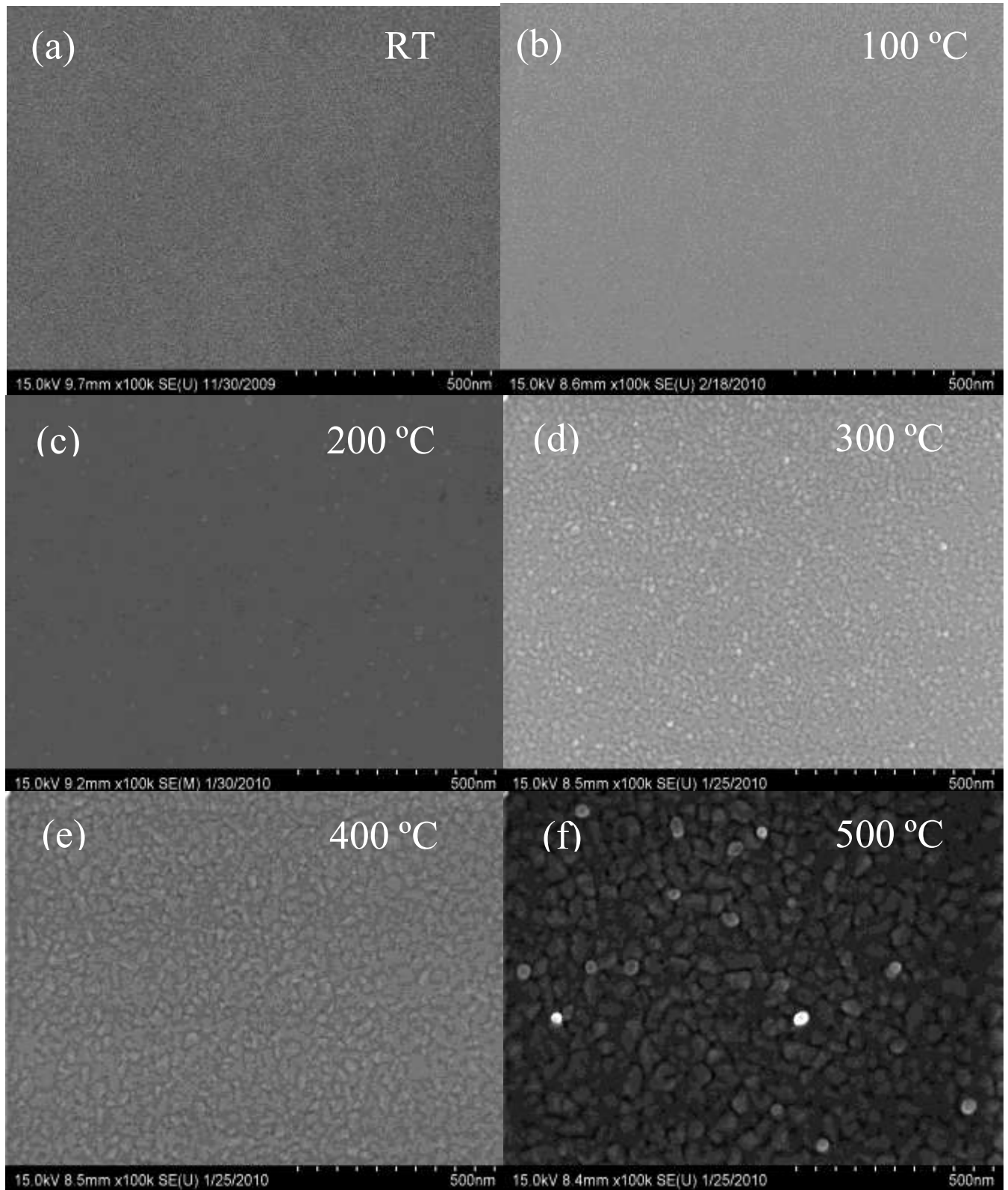
31

Figure 4.2: The high resolution SEM images of $W_{0.95}Ti_{0.05}O_3$ films grown at substrate temperatures (a) RT, (b) 100 ℃, (c) 200 ℃, (d) 300 ℃, (e) 400 ℃ and (f) 500 ℃.

32

The cross-sectional SEM images of $W_{0.95}Ti_{0.05}O_3$–Si interfaces for $W_{0.95}Ti_{0.05}O_3$ films grown at various temperatures are shown in Figure 4.3. The $W_{0.95}Ti_{0.05}O_3$ film and Si-substrate regions are as indicated in Figure 4.3 for a representative sample. The cross-sectional SEM images indicate that the $W_{0.95}Ti_{0.05}O_3$ films grow in a columnar structure on Si surfaces. The cross-sectional imaging analysis indicates that there is no reaction leading to compound formation at the Si–WO_3 interface even at the highest temperature (500 ºC).
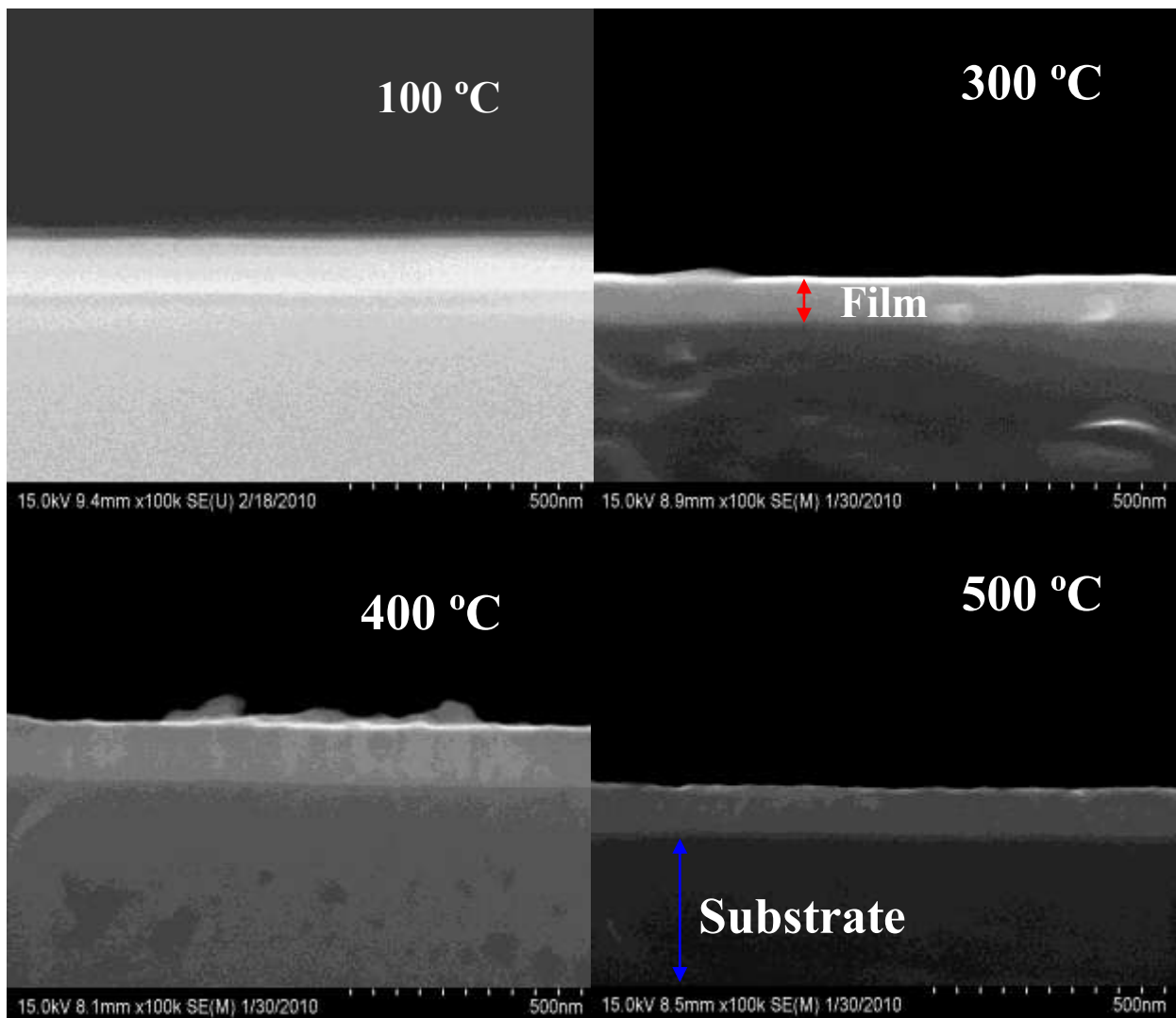

Figure 4.3: Si-$W_{0.95}Ti_{0.05}O_3$ cross-sectional SEM images of $W_{0.95}Ti_{0.05}O_3$ films grown at various temperatures. The Si substrate and $W_{0.95}Ti_{0.05}O_3$ film regions are indicated above.

The EDS spectra of representative $W_{0.95}Ti_{0.05}O_3$ films as a function of T_s are shown in Figure 4.4. The spectra indicate the characteristic x-ray peaks (as labeled in Figure 4.4) corresponding to W, Ti and O atoms present in the sample. The absence of any other peaks except those due to W, Ti and O indicate that the sample consists exclusively of W-Ti oxide phase. It is well-known that the x-rays generated are characteristic of the atoms (48). Therefore, the detection of x-rays emitted from the sample as a result of sample-electron beam interaction provides the identification of the atoms present in the crystal. The emitted x-ray peaks detected are only from W and O while the peak due to Si substrate is serving as a reference. No other elements were detected, which is a sign of high purity $W_{0.95}Ti_{0.05}O_3$ films without any elemental impurities incorporated from chemical processing or post-preparation handling.
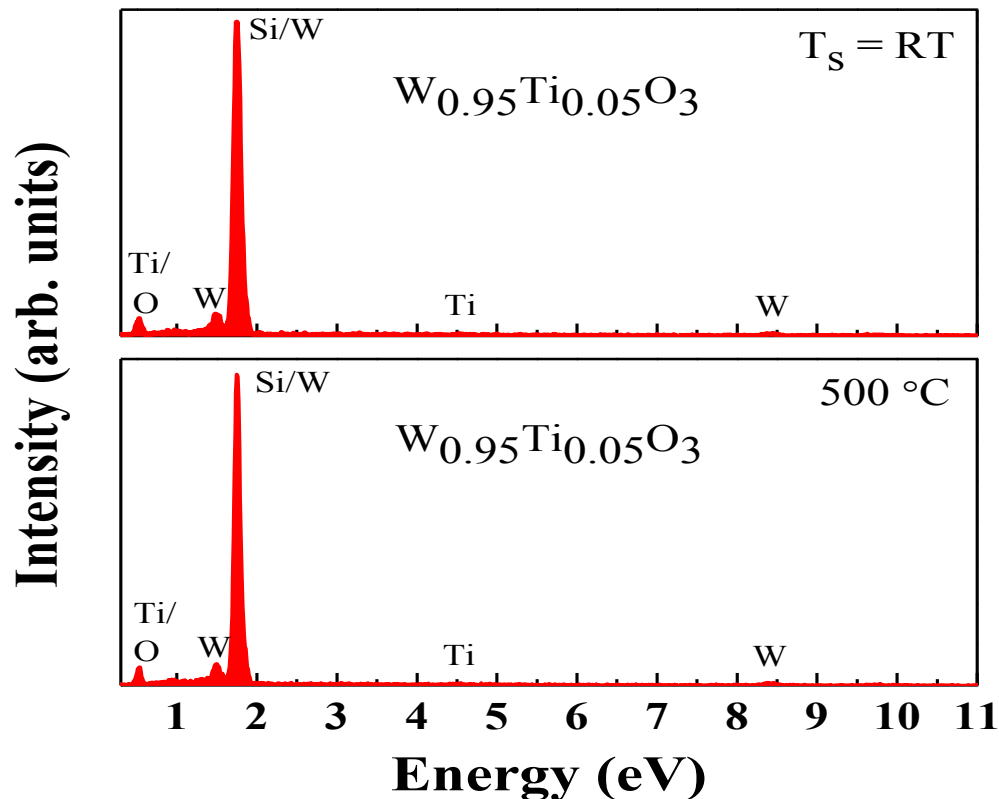

Figure 4.4: EDS spectra of $W_{0.95}Ti_{0.05}O_3$ films. The peaks due to x-rays emitted from W, Ti and O present in the films are as labeled

A phase diagram is proposed, based on the XRD, SEM, and EDS results, for the microstructure evolution of $W_{95}Ti_5O_3$ thin films as shown in Fig. 4.5. The phase diagram summarizes the observed structural changes as a function of substrate temperature and could provide a roadmap while considering the $W_{95}Ti_5O_3$ thin films for practical applications.
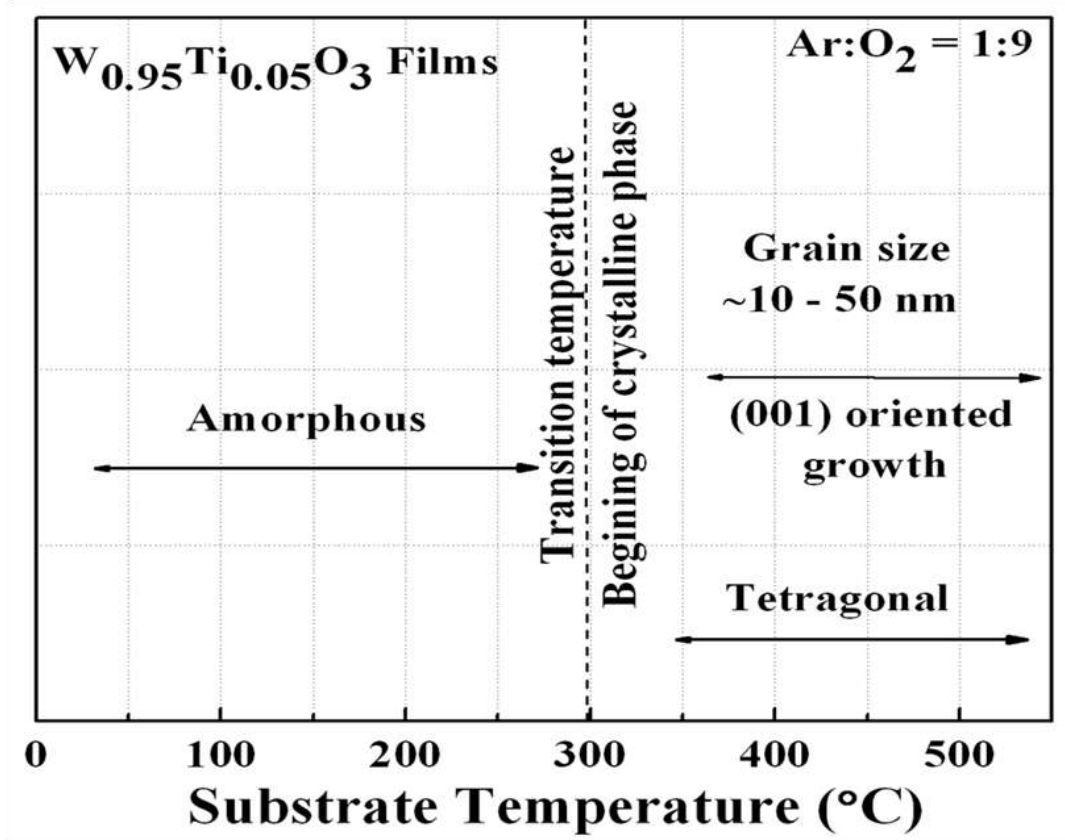
Figure 4.5: Phase diagram representing phase transformations as a function of substrate temperature

4.6 OPTICAL PROPERTIES

Transmittance spectra of all the $W_{0.95}Ti_{0.05}O_3$ films are shown in Figure 4.6. The spectra reveal two important characteristic features. 1. All the films are seen to exhibit very high transparency in the spectral region except where the incident radiation is absorbed across the band gap (E_g). 2. This observation indicates the high-quality and transparent nature of $W_{0.95}Ti_{0.05}O_3$ films with almost zero absorption losses.

35

It is well known that the optical absorption below E_g follows an exponential behavior. The absorption, therefore, is exponentially dependent on the energy ($h\upsilon$) of incident photon in that region. The graphs of absorption coefficient versus photon energy ($h\upsilon$) are studied to analyze the nature and value (E_g) of the band gap.

$$\alpha h\upsilon = B(h\upsilon - E_g)^2 \quad\text{................................}(11)$$

Where $h\upsilon$ is the energy of the incident photon, α is the absorption coefficient, B the absorption edge width parameter, Eg the band gap. The optical absorption coefficient, α, of the films is evaluated using the relation

$$\alpha = \left[\frac{1}{t}\right]\left[\ln\frac{T}{(1-R)^2}\right] \quad\text{...........................}(12)$$

Where T is the transmittance, R is the reflectance and t is the film thickness. The absorption data and the plots obtained for $W_{0.95}Ti_{0.05}O_3$ films are shown in Figure 4.7. Plot of $(\alpha h\upsilon)^{1/2}$ versus $h\upsilon$ would have a linear region with slope B and whose extrapolation to $\alpha (h\upsilon) = 0$ would give the value of E_g. E_g is found to decrease from 2.9 to 2.25 eV with increasing T_s which is shown in the Figure 4.8. The band gap value of $W_{0.95}Ti_{0.05}O_3$ films are less compare to that of pure WO_3 films. Increase in crystallization temperature and the structural disorder with the corporation of TiO_2 causes the decrease in band gap.

The second absorption at 3.1 eV and 3.0 eV corresponds to the TiO_2 phase has been observed in the case of films grown at 400 ºC and 500 ºC respectively as shown in Figure 4.7. The segregation of small amount of Ti ions at higher substrate temperature resulted in formation of small amount of TiO_2 phase. It is clear from structural studies that the Ti incorporation induces the disordering, inhibits the crystal growth and increases the crystallization temperature. The contribution to the optical absorption from the small amount of TiO_2 phase is evident from the Figure 4.7.
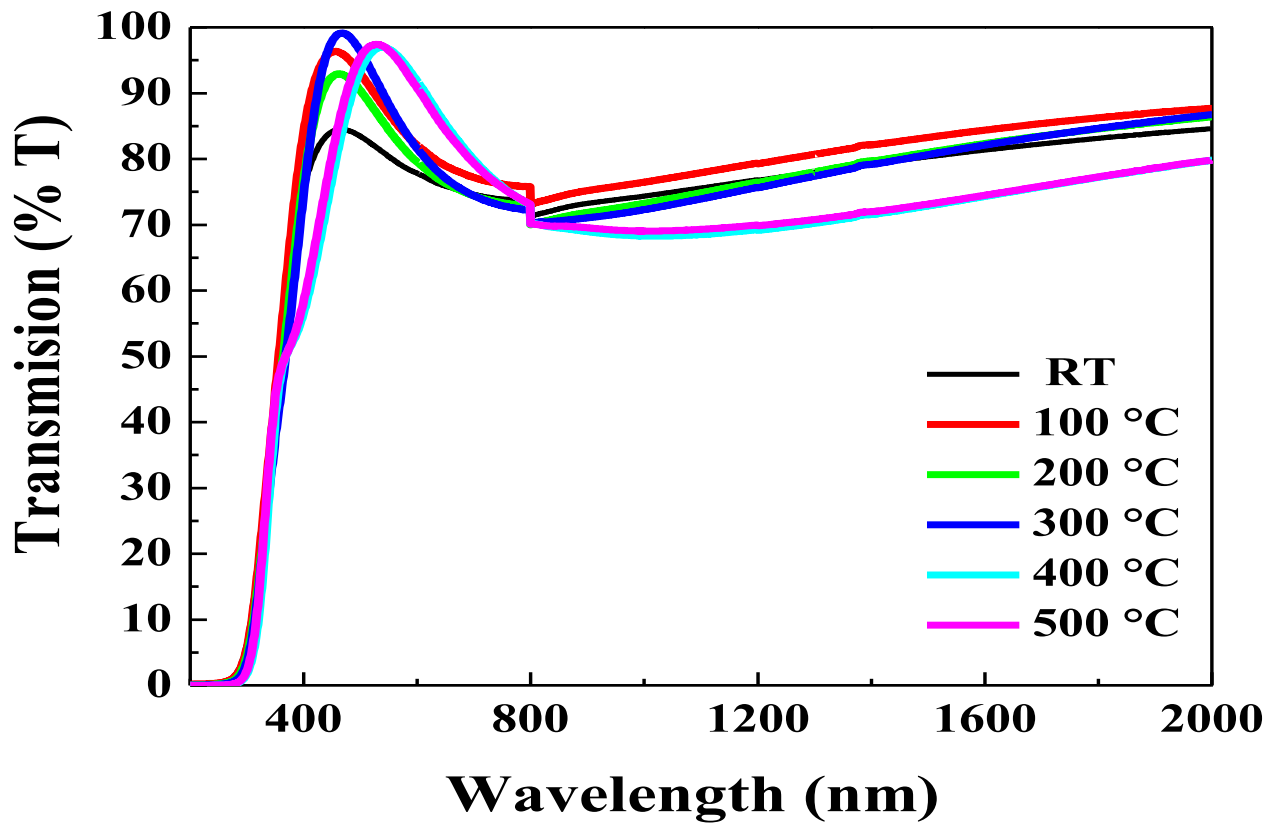
36

Figure 4.6: Optical transmittance spectra of $W_{0.95}Ti_{0.05}O_3$ films. The curves indicate that $W_{0.95}Ti_{0.05}O_3$ films are highly transparent

In the present case, the shift in E_g from 2.9 eV to 2.25 eV is due to the size-effect, which can theoretically be described based on strong or weak quantum confinement effect (QC). The strong QC regime is a case where the electrons and holes are independently confined when the size of a nanocrystal (R_n) is much smaller than the size of Bohr radius (R_B).

In the later case of weak QC, the energy is dominated by the Coulomb term and quantum effects arise from quantization of exciton motion. The E_g shift is relatively smaller in the latter case. In the present case, the $W_{0.95}Ti_{0.05}O_3$ nanocrystals exhibit a strong QC effect. The higher E_g for the film grown at RT, 100 ºC and 200 ºC is due to the amorphous nature of the films. E_g is seen to decrease with increasing the substrate temperature.
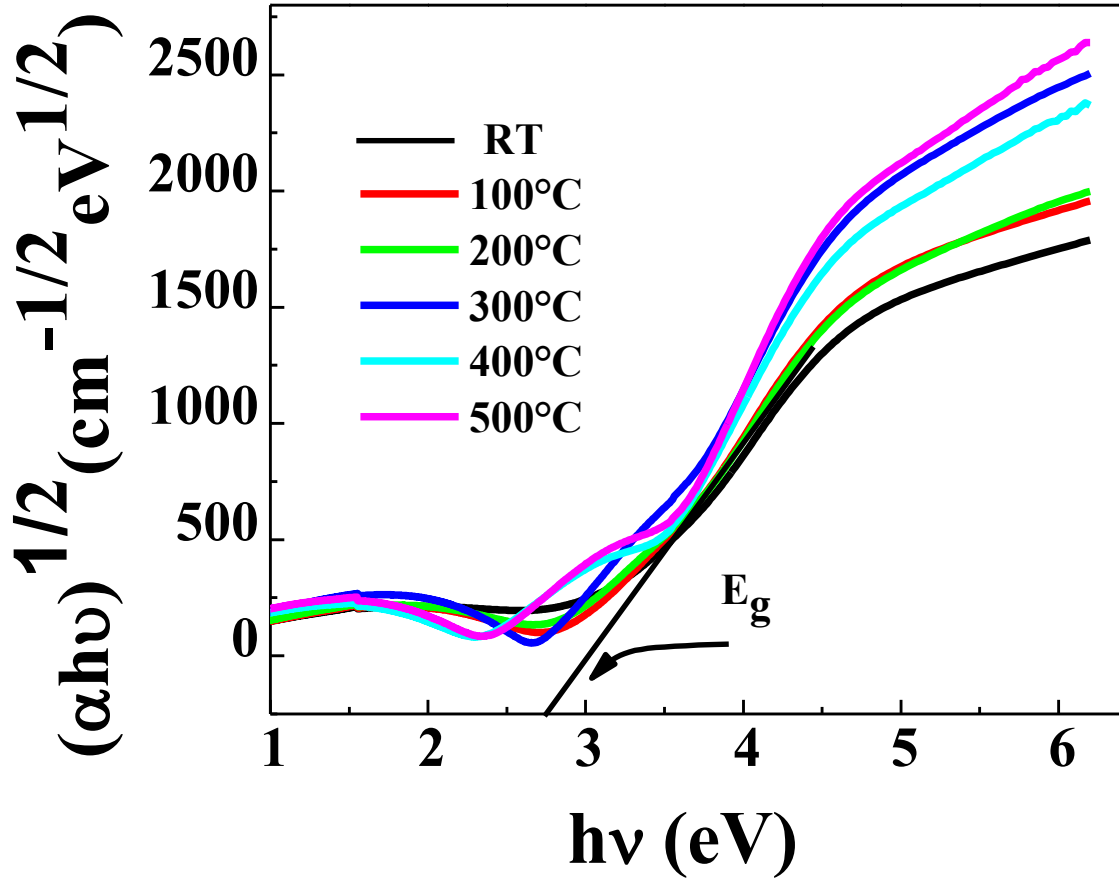
37

Figure 4.7: α vs. E for $W_{0.95}Ti_{0.05}O_3$ films. The extrapolation of the linear region to hν =0 to determine Eg values as indicated with line

4.7 ELECTRICAL RESISTIVITY

The room temperature electrical conductivity (σ) variation of $W_{0.95}Ti_{0.05}O_3$ films with T_s is shown in Figure 4.9. It can be seen that the σ increases with increasing T_s up to 400 ℃ which is due to improvement in the crystal structure of $W_{0.95}Ti_{0.05}O_3$ films. A small decrease in σ value at T_s=500 ℃ could be due to the formation of excess TiO_2 phase, as evidenced in XRD data. The σ is reported to decrease with size-reduction due to the increasing grain boundary volume and associated impedance to the flow of charge carriers. If the crystallite size is smaller than the electron mean free path, grain boundary scattering dominates and hence the conductivity decreases. The σ value is also very sensitive

to lattice imperfections in solids, such as vacancies and dislocations that are present in nanocrystalline materials.
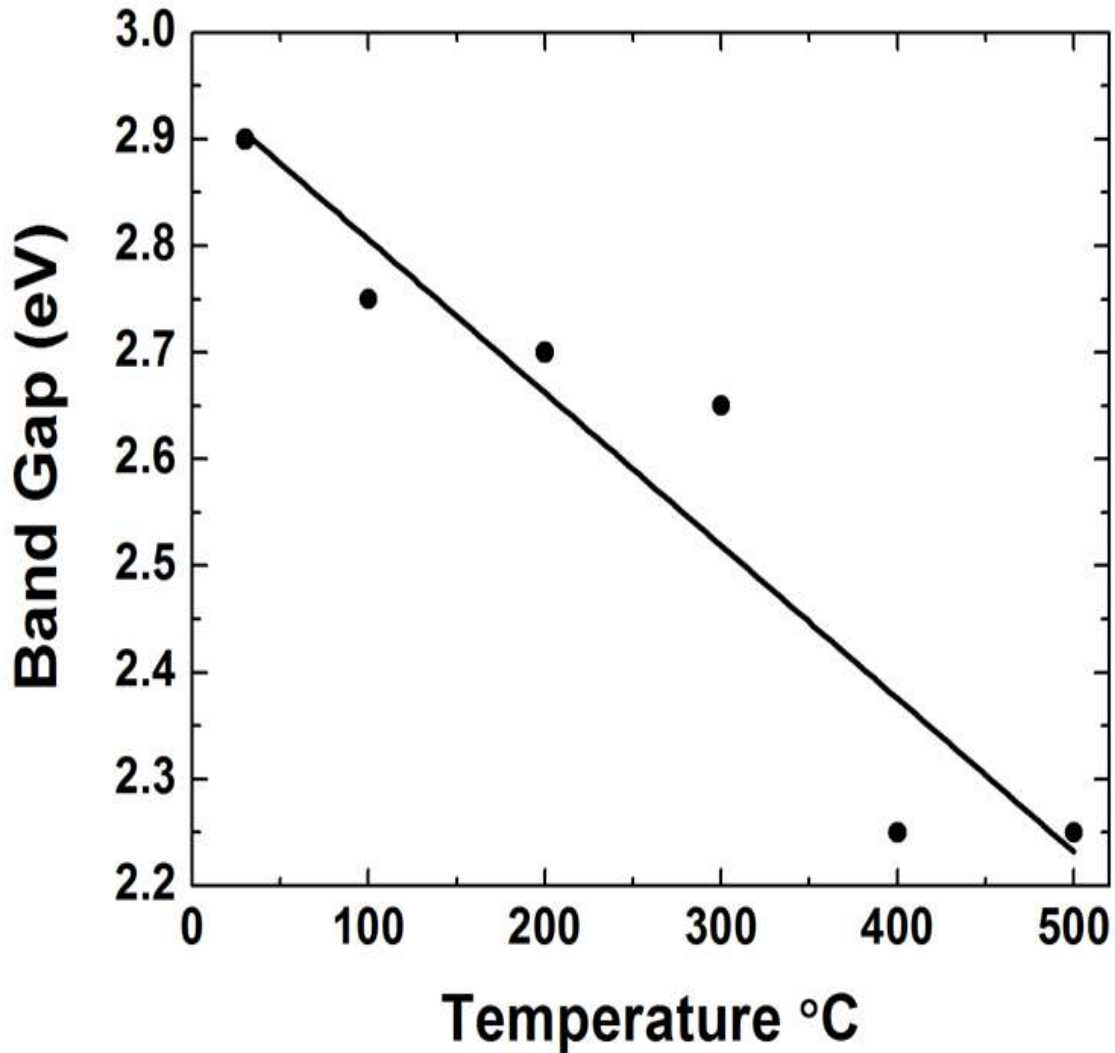
Figure 4.8: variation of band gap and refractive index of W0.95Ti0.05O3 films with substrate temperature

In addition to that, lattice strain and the distortions can affect the motion of charge causing decrease in conductivity. The σ-T_s data observed for $W_{0.95}Ti_{0.05}O_3$ can be explained taking these factors into consideration. $W_{0.95}Ti_{0.05}O_3$ films grown at T_s=RT-200 °C are amorphous. The randomness or disordered structure of the films induced by Ti, therefore, accounts for the observed low σ of a-$W_{0.95}Ti_{0.05}O_3$ films. An increase in σ with increasing T_s can be attributed to the structural transformation

39

from amorphous to tetragonal phase and preferred orientation of the film along (001). In addition, a decrease in strain energy of the growing $W_{0.95}Ti_{0.05}O_3$ film, as discussed using the XRD results, with increasing T_s also causes the increase in σ.

The temperature-dependent electrical conductivity plots of $W_{0.95}Ti_{0.05}O_3$ films are shown in Figure 4.10. Conductivity decreases exponentially with decreasing temperature from 300 to 80 K which indicates the semiconducting nature of all the $W_{0.95}Ti_{0.05}O_3$ films. However, a marked difference in the temperature-dependence of σ can be seen for a-$W_{0.95}Ti_{0.05}O_3$ films when compared to t-$W_{0.95}Ti_{0.05}O_3$ films. The most remarkable feature of these temperature-dependent electrical conductivity curves is the observation of two distinct regions indicative of two different conduction mechanisms operative in the
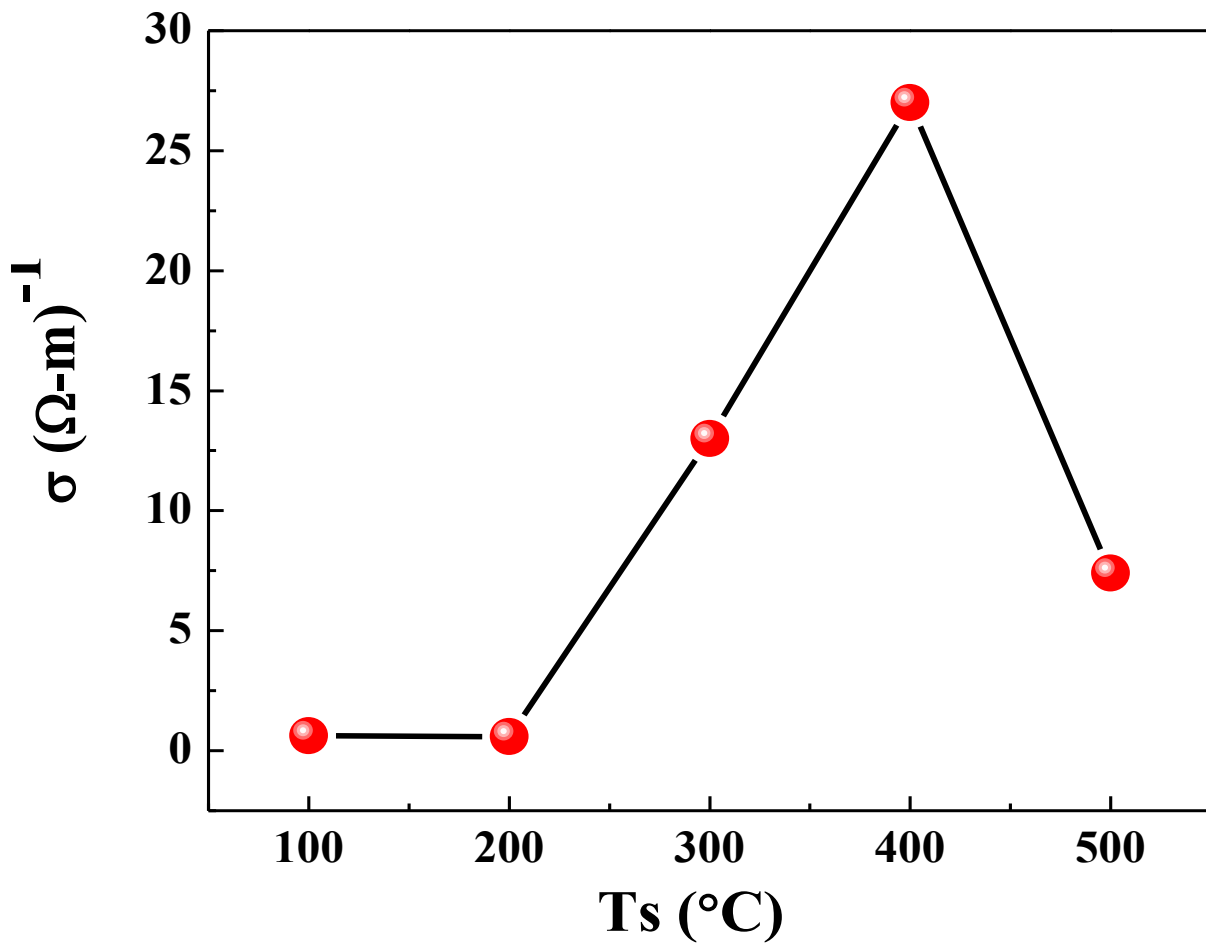

Figure 4.9: Room temperature electrical conductivity variation of $W_{0.95}Ti_{0.05}O_3$ films respective temperature regions.

40

Conductivity in semiconductors is due to both hopping of electrons and charge transport via excited states and it can be expressed as

$$\sigma = A_1 \exp\left(\frac{-E_1}{K_B T}\right) + A_2 \exp\left(\frac{-E_2}{K_B T}\right) + - - - A_n \exp\left(\frac{-E_n}{K_B T}\right) \quad \text{...........................} \quad (13)$$

Where E_1 is the activation energy for intrinsic conduction and $E_2 \ldots E_n$ are the activation energies needed for hopping conduction. $A_1, A_2 \ldots A_n$ are constants and k_B is the Boltzmann constant. Ln σ vs 1000/T plots yield two different slopes for $W_{0.95}Ti_{0.05}O_3$ films. The activation energy values at different temperature ranges (300-210 K and 210-80 K) calculated from the ln σ vs 1000/T plots are listed in Table 4. The activation energy is found to be higher in the 300-210 K temperature region (0.35 eV for the film grown at RT) when compared that in the 210-80 K temperature region (0.10 eV for the film grown at RT). Decreasing activation energy with decreasing temperature in transition metal oxides has been explained by small-polaron theory.

The variable range hopping (VRH) model of small polarons also predicts continuously decreasing activation energy with decreasing temperature. Small polaron formation occurs for strong enough electron–phonon interaction while the polaron transport occurs by a hopping process at sufficiently higher temperatures.

The multi phonon hopping process freezes out at lower temperatures, and conduction through extended states in a polaron band dominates. This should lead to a decay of the conductivity and activation energy as the temperature is reduced well below half of the Debye temperature. A simple model can be formulated to explain the observed results and to derive the microstructure-electrical property relationship in $W_{0.95}Ti_{0.05}O_3$ films. In order to do so we consider the simultaneous effect of Ti and T_s. It is clear from structural studies that the Ti incorporation induces the disordering, inhibits the crystal growth and increases the crystallization temperature.
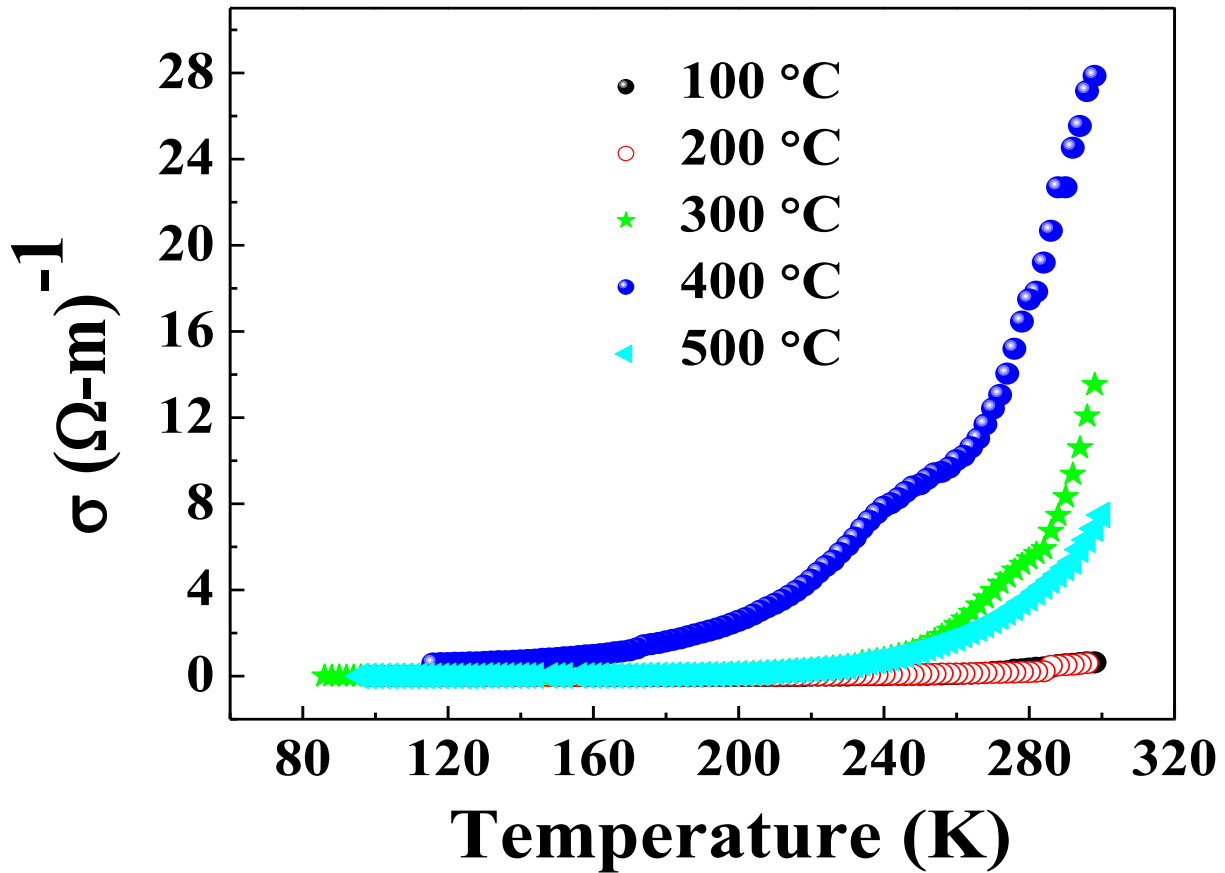
41

Figure 4.10: The temperature-dependent electrical conductivity plots of $W_{0.95}Ti_{0.05}O_3$ films

Therefore, a-$W_{0.95}Ti_{0.05}O_3$ films grown at T_s=RT-200 ºC exhibit a lower electrical conductivity. The physics behind this must be the changes in the chemical bonding and the co-ordination environment of W. The ideal WO_3 crystal structure can be represented as a cubic ReO_3 structure. Therefore, the structure is built up from a three-dimensional network of corner- sharing WO_6 octahedra. XRD results indicate the formation of a small amount of the TiO_2 phase at T_s>400 ºC. Therefore, the disordering in $W_{0.95}Ti_{0.05}O_3$ can be attributed to breaking the ordering of WO_6 octahedron by Ti by partially substitution for W atoms. The corner sharing Ti ions in WO_6 octahedra segregate to the surface upon increasing T_s resulting in the formation of a TiO_2 phase. A clear evidence for this hypothesis is the broadening of the XRD peak for $W_{0.95}Ti_{0.05}O_3$ films grown at T_s=500 ºC accompanied by a decrease in electrical conductivity. However, the initial rise in conductivity for $W_{0.95}Ti_{0.05}O_3$ films grown at T_s=RT-400 ºC is due to improved structural order where the Ti distortion and segregation is not dominant.

42

Table 4: Activation energy values calculated from the ln σ vs. 1000/T plots of W0.95Ti0.05O3 thin films for different temperature regions.

	Activation Energy (eV)	
T_s	300 – 210 K	210 – 80 K
100 ˚C	0.35	0.10
200 ˚C	0.36	0.11
300 ˚C	0.34	0.08
400 ˚C	0.34	0.08
500 ˚C	0.35	0.09

Chapter 5: Summary and Conclusions

Summarizing the results, $W_{0.95}Ti_{0.05}O_3$ films were fabricated using sputter-deposition and their crystal structure, phase, surface and interface morphology, chemical quality, and optical and electrical properties were investigated. The disordering effect induced by Ti is evident in microstructure, optical and electrical properties of $W_{0.95}Ti_{0.05}O_3$ films. The effect is pronounced by amorphization and elevating the crystallization temperature of $W_{0.95}Ti_{0.05}O_3$ films. The transformation is characterized by a transition from disordered to tetragonal structure. Associated with the disordering effect and structural transition, a marked difference in the temperature-dependence of conductivity is evident for a-$W_{0.95}Ti_{0.05}O_3$ films when compared to t-$W_{0.95}Ti_{0.05}O_3$ films. The crystal growth inhibiting effect of Ti can be useful to tailor the specific phase and size of WO_3 crystalline films for the desired applications. The EDS data confirm the formation of high purity $W_{0.95}Ti_{0.05}O_3$ films without any elemental impurities incorporated from chemical processing or post-preparation handling. Room temperature electrical conductivity of $W_{0.95}Ti_{0.05}O_3$ films increases from 0.63 $(\Omega\text{-cm})^{-1}$ to 27 $(\Omega\text{-cm})^{-1}$ with increasing temperature from RT to 400 ^{o}C due to improved structural order. The observed decrease in electrical conductivity at 500 ^{o}C (7.4 $(\Omega\text{-cm})^{-1}$) is due to disordering induced by Ti segregation, which is confirmed by XRD. The optical band gap was found to be decreasing with Ti incorporation. However, at higher temperatures (400-500 ^{o}C), a second absorption band with a higher energy gap closer to that of TiO_2 evidences the segregation and formation of titanium oxides on the film surfaces. Based on the results obtained in this work, a phase diagram for the microstructure evolution in $W_{0.95}Ti_{0.05}O_3$ thin films is proposed.

Chapter 5: Future work

The scope and suggestions for the future work are listed below

1. The optimized conditions from this work can be used to develop W-Ti-O based H_2S sensors.

2. The electrical properties of pure W-Ti-O films can be investigated using a sensor setup in the presence of H_2S.

3. The long-term stability and poisoning of the materials under exposure to H_2S can be tested.

4. Increasing the concentration of Ti above 5% can be explored. It will be interesting to see how the higher Ti concentrations influences the fundamental aspects of WO_3 compared to results documented on pure WO_3 and results presented in this thesis on 5% Ti-doped WO_3 materials.

References

1. A. J, Minchener. "Coal gasification for advanced power generation." *Fuel* 84 (2005).

2. Smoot, L Douglas, and Philip J Smith. *Coal, coal gasification; combustion.* New York: Plenum Press, (1985).

3. Hobbs, M L, T Radulovic P, and D Smoot L. "Combustion and gasification of coals in fixed beds; progress in energy and combustion sciences." Review, (1993), 505-586.

4. Smoot, L D. *Fundamentals of coal combustion.* The Netherlands: Elsevier, (1993).

5. Attar, A. "Chemistry thermodynamics and kinetics of reactions of sulphur in coal-gas reactions: A review." *Fuel*, (1978): 201-212.

6. Thompson, F C, and N Tilting. *J. Soc. Chem. Ind,* 53 (1924): 37-46.

7. H, Lin, Hsu C, Yang H, Lee P, and Yang C. "Nanocrystalline WO_3-based H_2S sensors." *Sens. Actuators B* 22 (1994): 63-68.

8. George, Fine F, Leon M. Cavanagh, Ayo Afonja, and Russell Binions. "Metal Oxide Semi-Conductor Gas Sensors in Environmental Monitoring." *Sensors*, (2010): 5469-5502.

9. H, Meixner, Gerblinger J, Lampe U, and Fleischer M. "Thin-film gas sensor based in semiconductor metal oxides." *Sens. Actuators B* 23 (1995): 119-125.

10. Isolde Simon, Nicolae BaÃrsan, Michael Bauer, and Udo Weimar. "Micromachined metal oxide gas sensors: opportunities to improve sensor performance." *Sensors and Actuators B* (2001): 1-26.

11. Hooker, Stephanie A. "Nanotechnology Advantages Applied to Gas Sensor Development." *The Nanoparticles 2002 Conference Proceedings.* (2002). 1-7.

12. J, Solis, Saukko S, Kish L, Granqvist C, and Lantto V. "Nanocrystalline tungsten oxide thick-films with high sensitivity to H_2S at room temperature." *Sens. Actuators B* 77 (2001): 316-321.

13. N, Barsan, and Weimer U. "Understanding the fundamental priciples of metal oxide based gas sensors; the example of CO sensing with SnO_2 sensors in the presence of humidity." *J. Phys. Cond. Matt.,* 15 (2003): R813.

14. P. A, Cox. *Transition Metal Oxides.* Vol. Clarendon Press. Oxford.

15. E, Comini, Sberveglieri G, and Guidi V. "Ti–W–O sputtered thin film as n- or p-type gas sensors." *Sensors and Actuators B*, (2000): 108–114.

16. D, Smith, Vetelino J, Falconer R, and Wittman E. "Stability, sensitivity and selectivity of tungsten trioxide films for sensing applications." *Sens. Actuators B* 13-14 (1993): 264-268.

17. M, Ferroni, Guidi V, Martinelli G, Nelli P, and Sberveglieri G. "Gas-sensing applications of W–Ti–O-based nanosized thin films." *Sensors and Actuators B*, (1997): 499–502.

18. O. K, Varghese, and Grimes C. A. "Metal oxide nanoarchitectures for environmental sensing." *J. Nanosci. Nanotech.* 3 (2003): 377.

19. J, Solis, Saukko S, Kish L, Granqvist C, and Lantto V. "Semiconductor gas sensors based on nanostructured tungsten oxide." *Thin Solid films* 391 (2001): 255-260.

20. E, Saljie, and Viswanathan K. "Physical properties and phase transitions in WO_3." *Acta Crystallogr. A* 31 (1975): 356-359.

21. G. N, Chaudhari, Bende A. M, Bodade A. B, Patil S. S, and Sapkal V. S. "Structural and gas sensing properties of nanocrystalline TiO_2: WO_3-based hydrogen sensors." *Sens. Actuators B* 115 (2006): 297-302.

22. N, Taguichi. Jpn Patent 45-38200. (1962).

23. Siyama, T., Kato A, Fujiishi K, and Nagatani M. "A new detector for gaseous components using semiconducting thin films." *Anal. Chem.*, (1962): 1502-1503.

24. N, Taguichi. UK Patent 1280809. (1970).

25. Alexey, Tomchenko A, P Harmer Gregory, T Marquis Brent, and W Allen John. "Semiconductor metal oxide sensor array for the selective detection of combustion gases." *Sens. Actuators B* 93 (2003): 126-134.

26. J, Tamaki, et al. "Grain-size effects in tungsten oxide-based sensor for nitrogen oxides." *J. Electrochem. Soc.* 141 (1994): 2207-2210.

27. B, Fruhberger, Grunze M, and Dwyer D. J. "Surface chemistry of H_2S-sensitive tungsten oxide films." *Sens. Actuators B* 31 (1996): 167-174.

28. M, Antonik, Schneider J, Wittman E, Snow K, Vetelino J, and Lad R. "Microstructural effects in WO_3 gas-sensing films." *Thin Solid Films* 256 (1995): 247-252.

29. S, Moulzolf, Ding S, and Lad R. "Stoichiometry and microstructure effects on tungsten oxide chemiresistive films." *Sens. Actuators B* 77 (2001): 375-382.

30. S, Santucci, Cantalini C, Crivellari M, Lozzi L, Ottaviano L, and Passacantando M. "X-rat photoemission spectroscopy and scanning tunnelling spectroscopy on the thermal stability of WO_3 thin films." *J. Vac. Sci. Technol. A* 18 (2000): 1077-1082.

31. W, Tao, and Tsai C. "H_2S sensing properties of noble metal doped WO_3 thin film sensor fabricated by micromachining." *Sens. Actuators B* 81 (2002): 237-247.

32. P. J, Shaver. "Activated tungsten oxide gas detectors." *Appl. Phys. Lett.* 11 (1967): 255-257.

33. Depero, Groppelli S, Natali-Sora I, Sangaletti L, Sberveglieri G, and Tondello E. "Structural studies of tungsten-titanium oxide thin films." *J. Sol. State Chem.* 121 (1996): 379-387.

34. C, Bittencourt, et al. "Effects of oxygen partial pressure and annealing temperature on the formation of sputtered tungsten oxide films." *J. Electrchem. Soc.* 149 (2002): H81-H86.

35. C, Cantalini, Lozzi L, Passacantando M, and Santucci S. "The comparative effect of two different annealing temperatures and times on the sensitivity and long-term stability of WO_3 thin films for detecting NO_2." *IEEE Sensors Journal* 3 (2003): 171-179.

36. E, Barrett, Georgiades G, and Sermon P. "The mechanism of operation of WO_3-based H_2S sensors." *Sens. Actuators B* 1 (1990): 116-120.

37. C. V, Ramana, Utsunomiya S, Ewing R. C, Julien C. M, and Becker U. "Structural stability and phase transitions in WO_3 thin films." *J. Phys. Chem. B* 110 (2006): 10430.

38. Avner Rothschild, and Yigal Komem. "The effect of grain size on the sensitivity of nanocrystalline metal-oxide gas sensors." *Journal of Applied Physics*, (2004): 6374-6380.

39. L, Sangaletti, Depero L. E., Sberveglieri G, Allieri B, Bontempi E, and Groppelli S. "Growth of WO3 crystals from W-Ti-O thin films." *Journal of Crystal Growth*, 1240-1244: 1999.

40. L. E., Depero, Groppelli S, Natali-Sora I, Sangaletti L, Sberveglieri G, and Tondello E. "Structural Studies of Tungsten–Titanium Oxide Thin Films." *Journal of Sloid state Chemistry*, 1996: 379–387.

41. M, Ferroni, et al. "Nanosized thin films of tungsten-titanium mixed oxides as gas sensors." *Sensors and Actuators B*, 1999: 289–294.

42. L. E., Depero, Natali Sora I, Perego C, Sangaletti L, and Sberveglieri G. "Kinetics of disorder-order transition of Ti-W oxide thin-film sensors." *Sensors and Actuators B*, 1996: 19-24.

43. N, Bundaleski, Petrovic S, Perusko D, Kovac J, and Zalar A. "Composition of the sputter deposited W–Ti thin films." *Applied Surface Science*, 2008: 6390–6394.

44. S, Petrovic, et al. "Surface analysis of the nanostructured W–Ti thin film deposited on silicon." *Applied Surface Science*, (2007): 5196–5202.

45. S. K., Gullapalli, Vemuri R. S., and Ramana C. V. "Structural transformation induced changes in the optical properties of nanocrystalline tungsten oxide thin films." *Applied Physics Letters*, 2010: 171903-3.

46. S. K., Gullapalli, Vemuri R. S., Manciu F. S., Enriquez J. L., and Ramana C. V. "Tungsten oxide (WO_3) thin films for application in advanced energy systems." *J. Vac. Sci. Technol. A*, 2010: 824-828.

47. C. V, Ramana, Vemuri R. S, Fernandez I, and Campbell A. L. "Size-effects on the optical properties of zirconium oxide thin films." *Appl. Phys. Lett.* 95 (2009): 231905.

48. Mitrivics, J, H Ulmer, U Weimar, and W Gopel. *Acc. Chem. Res* 31 (1998): 307-315.

Vita

Narasimha Raju Kalidindi was born on October 15th, 1986 in Hyderabad, Andhra Pradesh, India. The first son of Krishna Bhagavan Raju Kalidindi and Leela Kumari Kalidindi, he graduated from Jawaharlal Nehru Technological University with a bachelor's degree in Mechanical Engineering. He then travelled to El Paso, Texas to pursue his master's degree from the University of Texas at El Paso in Mechanical Engineering. During his master's, he worked as a research assistant in the department of mechanical engineering. In fall 2010, he graduated with a Master of Science degree in Mechanical Engineering.

Permanent address: H-NO: 1-72, Besides DRF East Gate, Bollarm Road, Miyapur

Hyderabad, Andhra Pradesh, 500050.